



HAL
open science

Sulfur, selenium and tellurium fractionation during magma crystallization and degassing: constraints from southwest Indian Ocean volcanism (La Réunion Island and Fani Maoré volcano, Mayotte)

Ivan Vlastélic, Jean-Luc Piro, Vincent Famin, Carole Berthod, Patrick Bachèlery, Thomas Rouyer, Andrea Dimuro

► To cite this version:

Ivan Vlastélic, Jean-Luc Piro, Vincent Famin, Carole Berthod, Patrick Bachèlery, et al.. Sulfur, selenium and tellurium fractionation during magma crystallization and degassing: constraints from southwest Indian Ocean volcanism (La Réunion Island and Fani Maoré volcano, Mayotte). 2024. hal-04745393v2

HAL Id: hal-04745393

<https://hal.science/hal-04745393v2>

Preprint submitted on 23 Oct 2024

HAL is a multi-disciplinary open access archive for the deposit and dissemination of scientific research documents, whether they are published or not. The documents may come from teaching and research institutions in France or abroad, or from public or private research centers.

L'archive ouverte pluridisciplinaire **HAL**, est destinée au dépôt et à la diffusion de documents scientifiques de niveau recherche, publiés ou non, émanant des établissements d'enseignement et de recherche français ou étrangers, des laboratoires publics ou privés.

1 **Sulfur, selenium and tellurium fractionation during magma crystallization and**
2 **degassing: constraints from southwest Indian Ocean volcanism (La Réunion**
3 **Island and Fani Maoré volcano, Mayotte)**

4

5

6

7

8 I. Vlastélic^{1,2, *}, J.-L. Piro¹, V. Famin^{2,3}, C. Berthod², P. Bachèlery¹, T. Rouyer¹, A. Di Muro⁴

9

10

11 1 Université Clermont Auvergne, CNRS, IRD, OPGC, Laboratoire Magmas et Volcans, F-63000
12 Clermont-Ferrand, France

13

14 2 Université Paris-Cité, Institut de physique du globe de Paris, CNRS, UMR 7154, F-75005 Paris,
15 France

16

17 3 Université de La Réunion, Laboratoire GéoSciences Réunion, F-97744 Saint-Denis, France

18

19 4 Laboratoire de Géologie de Lyon Terre - Planètes – Environnement, Observatoire de Lyon,
20 UAR 3721 COMET

21

22

23 • Corresponding author

24

25 Word count: 6752 (text body)

26

27 **Abstract**

28

29 Selenium (Se) and tellurium (Te) are oxygen group elements that share chemical properties
30 with sulfur, but also show subtle differences that are useful to constrain magmas genesis and
31 source. Using high-precision isotope dilution measurements, this study characterizes the
32 behavior of Se and Te, relatively to S, during the degassing and crystallization of cogenetic
33 magmas from the southwest Indian Ocean. The study of subaerial and submarine lavas from
34 La Réunion Island first shows that, unlike S and Te, Se is not significantly lost during the rapid,
35 final ascent of less differentiated magmas ($\text{MgO} > 6\text{wt}\%$). This is because Se is retained as
36 selenide in primary melts despite relatively oxidized conditions. Conversely, selenium
37 degassing occurs during magma crystallization below 6 wt% MgO, at a similar rate as sulfur,
38 yielding small S/Se fractionation in the residual magma. Sulfide fractionation, which begins
39 between 5 and 4 wt% MgO, has minor effect on Se compared to Cu. Tellurium is extensively
40 outgassed from La Réunion subaerial lavas but shows a very specific behavior in submarine
41 lavas where it is retained and even accumulate near 6 wt% MgO. The very different behaviors
42 of Se and Te during magma degassing yields extremely large Se/Te variations between
43 subaerial (up to 225) and submarine (down to 1) lavas from La Réunion.

44 The Fani Maoré eruption that occurred between 2018 and 2021 offshore the island of Mayotte
45 (Comoros Archipelago) also provided the opportunity to study chalcogens degassing during
46 the emplacement of submarine lavas. The study of a pillow lava showing a radial textural
47 zonation typical of degassing-crystallization during cooling reveals that S, Se and other
48 moderately volatile elements (Mo, W, Cs) are the most depleted at intermediate depth within
49 the pillow where pipe vesicles occur, suggesting these elements escape with major volatiles.
50 Conversely, Te is depleted in the whole interior of the pillow, suggesting Te is more efficiently
51 lost due to a lower solubility in magma. Assessment of pillow degassing during emplacement
52 yields a 6.5% loss of the initial S content, 7.2% for Te, but only 1.6% for Se confirming the lower
53 volatility of Se during lava emplacement. Chalcogens degassing is accompanied with
54 significant loss of W (8.9%), Mo (5.1%) and Cs (5.1%) from Fani Maoré lavas. Based on these
55 values, the 6.5 km^3 Fani Maoré eruption released $1.1 - 1.5 \times 10^6$ tons of S, 2300 – 2700 tons
56 of Mo, 970 – 1130 tons of W, 194 – 339 tons of Cs, 13.3 – 16 tons of Se and 4.5 – 11.8 tons of
57 Te during emplacement.

58 The unusually elevated S/Se ratios (16929 – 22130) of Fani Maoré lavas requires a mantle
59 source extensively fertilized by sulfide melts, whereas the reconstructed S – Se – Te
60 composition of La Réunion plume source is consistent with the preservation of chondritic S/Se
61 and Se/Te ratios.

62

63 Keywords : selenium, tellurium, magma degassing, magma differentiation, La Réunion,
64 Mayotte, Fani Maoré eruption

65 1. Introduction

66

67 Selenium (Se) and tellurium (Te) are group 16 elements sharing chemical and physical
68 properties with the element sulfur. In particular S^{2-} , Se^{2-} and Te^{2-} have very similar ionic radii
69 (Shannon et al., 1976) allowing extensive substitution in reducing conditions. These elements
70 are the object of a growing interest because Se and Te are useful elements to constrain models
71 of Earth accretion and differentiation (Wang and Becker, 2013), upper mantle processes such
72 partial melting and refertilization of the lithosphere (Lorand and Allard, 2010; König et al.,
73 2012), while Se plays an important role in biogeochemical cycle (Sharma et al., 2015).
74 Selenium and tellurium are highly volatile elements but also tend to substitute for sulfur in
75 immiscible sulfide liquids. This dual nature led to different views regarding the fate Se and Te
76 during magma genesis and eruption. On the one hand, studies of mantle rocks, ultramafic
77 cumulates and lavas show that Se and Te are trapped in dense sulfides that accumulate in the
78 deep roots of volcanoes (Hertogen et al., 1980; Lissner et al., 2014; Collins et al., 2012; Yierpan
79 et al., 2019). On the other hand, studies of more-or-less degassed lavas (Yierpan et al., 2021)
80 and volcanic gas products (Greenland and Aruscavage; 1986; Zelenski et al., 2021; Rosca et al.,
81 2021) show that Se and Te extensively partition into the vapor phase and are delivered to the
82 outer layers of the Earth. At the heart of this debate is the timing of sulfide saturation relative
83 to magma degassing, and the degree to which Se and Te partition into sulfide melts relative
84 to the gas phase. Edmonds et al. (2018) suggest that sulfide saturation control the metal
85 signature of volcanic gas, and its variations in arc and hotspot settings. Conversely, Zelenski et
86 al. (2021) suggest that the trace element budget of volcanic gas is mainly determined by the
87 near-surface partitioning of elements between gas and silicate melt.

88 This paper investigates the S – Se – Te signature of La Réunion hotspot magmatic system to
89 constrain the nature of the hotspot source, and the role of sulfide saturation versus degassing
90 on the composition of the erupted lavas. Our approach is based on the study of cogenetic
91 rocks including plutonic rocks and lavas showing a wide range of degassing (submarine and
92 subaerial) and crystallization (basalt to trachyte) extents, as well as contrasted cooling rates
93 (lava flow and glassy tephra). We also compare the S – Se – Te signature of the low-pressure
94 Réunion magmas to the signature of the high-pressure sulfide saturated magmas that were
95 emitted during the 2018-2021 Fani Maoré eruption offshore the Mayotte Island (Berthod et
96 al., 2021, 2022). The results show that the residual abundances of S, Se and Te in lavas are

97 dominantly controlled by degassing processes, unlike less volatile Cu, which records the
98 deeper processes of sulfide saturation.

99

100 2. Geological setting

101

102 The island of La Réunion (Indian Ocean) is the present location of the hotspot that created the
103 Deccan traps ca. 66 Ma ago (Fig. 1a). The oldest submarine activity is dated at 3.8 Ma
104 (Smietana, 2011), but the edifice most likely started to grow ca. 5 Myr ago (Bonneville et.,
105 1988). The emergent part of the island comprises a quiescent volcano (Piton des Neiges) in
106 the NW and a basaltic shield volcano (Piton de la Fournaise) in the SE (Fig. 1b). Piton des Neiges
107 produced olivine basalts between 2.1 and 0.43 Ma ago, and increasingly differentiated lavas
108 (hawaiite, benmoreite, mugearite and trachyte) until its final activity ca. 27 ka ago (Upton and
109 Wadsworth, 1972; Gillot and Nativel, 1982; Famin et al., 2022). Piton de la Fournaise has been
110 regularly active since at least 400-450 ka (Gillot and Nativel, 1989; Merle et al., 2010) and is
111 still presently in its shield building stage. This volcano, one of the most regularly active of the
112 planet, is well known for producing olivine basalts with little compositional variability
113 (Albarède et al., 1997; Vlastélic et al., 2018).

114 Mayotte is one of the four islands of the Comoros Archipelago located between Africa and
115 Madagascar (Fig. 1a). The origin of Comoros volcanism is debated and could either be related
116 to a mantle plume or to lithosphere deformation (Hajash and Armstrong, 1972; Emerick and
117 Duncan, 1982; Class et al., 2005; Nougier et al., 1986; Famin et al., 2020; Feuillet et al., 2021;
118 Thinon et al., 2022). The Fani Maoré submarine eruption occurred between 2018 and 2021,
119 50 km east of Mayotte, along the East-Mayotte submarine Volcanic Chain, on a 3300 m-deep
120 seafloor (Fig. 1c). The eruption produced 6.5 km³ of homogeneous basanitic magmas during
121 three main eruption phases related to different magma paths (Berthod et al., 2021, 2022;
122 Chauvel et al. 2024).

123

124 3. Samples

125

126 La Réunion sample set, summarized in table 1 and displayed in figure 1b, is composed of: (1)
127 twelve co-genetic samples from the Piton des Neiges differentiation suite, including three
128 olivine-basalts, two hawaiites, two benmoreites and five trachytes. These samples cover all

129 four magmatic stages of Piton des Neiges (Upton and Wadsworth, 1972; Gillot and Nativel,
130 1982) and were previously selected and studied by Famin et al. (2016), Nauret et al. (2019),
131 and Berthod et al. (2020). All these samples were collected on land, some emplaced as lava
132 flows and others as sheet intrusions; (2) three plutonic rocks with wehrlitic composition (33 –
133 41.5 wt% MgO) interpreted as magma chamber cumulates (Barrat and Bachèlery, 2019;
134 Berthod et al., 2020); (3) nine lava samples from the recent (2007-2020) activity of Piton de la
135 Fournaise volcano studied by Vlastélic et al. (2013), including eight basalts with a
136 homogeneous MgO content (6.4 to 8 wt%), and one olivine-rich lava (29.2 wt% MgO). These
137 samples were selected to cover a wide range of textures and cooling rates (crystallized lava,
138 quenched lava, scoria, pumice, Pele's hairs). (4) Ten submarine lavas, including four samples
139 related to the early history of Piton des Neiges, and six lavas related to the submarine
140 volcanism that occurred in the southeast of the island prior to Piton de la Fournaise. These
141 samples have MgO content between 5.1 and 13 wt% (Smietana et al., 2010; Smietana, 2011).
142 The Fani Maoré samples selected for this study are all fresh submarine lavas studied by
143 Berthod et al. (2021, 2022) and Chauvel et al. (2024). The samples were dredged during
144 MAYOBS (Rinnert et al., 2019) and GEOFLAMME cruises (Rinnert et al., 2021). Dredge
145 locations are reported in [table 1](#) and displayed in [figure 1c](#). Samples include: (1) eight evolved
146 basanites covering the three main phases of the 2018-2021 submarine eruption ([Table 1](#)).
147 Except for one sample with 9.9 wt% MgO, the eight samples display small compositional
148 variations ($3.8 \leq \text{MgO} \leq 4.8$ wt%) ascribed to magma differentiation in a large (≥ 10 km³)
149 reservoir located within the lithospheric mantle (Berthod et al., 2021). Bulk porosity decreases
150 from 30 – 45% during phase 1 to 5 – 20% during phase 3 (Verdurme et al., 2024). Sulfides
151 droplets occur in all these samples and are most abundant in the third phase samples (Berthod
152 et al., 2022). (2) Nine samples regularly drilled from the glassy margin to the core of a pillow
153 lava ([Fig. 2](#)) erupted during the third phase of the 2018-2021 eruption (sample GFL-DR20-0101
154 in Berthod et al., 2022, with MgO of 4.45 wt%).

155

156 4. Analytical methods

157

158 Selenium and tellurium concentrations were analyzed by isotope dilution (ID) hydride
159 generation (HG) quadrupole inductively coupled plasma mass spectrometry (ICP-MS)
160 following a method modified from Yierpan et al. (2018). We first prepared ⁷⁷Se enriched

161 (44.773 ppb Se with 94.38% ^{77}Se) and ^{125}Te enriched (5.214 ppb Te with 95.52% ^{125}Te) spike
162 solutions from solid sources obtained from Oak Ridge National Laboratory, USA. The
163 concentrations of the spike solutions were calibrated by isotope dilution against solutions
164 prepared by diluting a 10 $\mu\text{g/g}$ certified standards from Inorganic Venture. The spikes
165 concentrations were obtained by averaging the measurements of three spike-standard
166 mixtures prepared around the spike/standard optimal ratio. For sample analysis, 200 mg of
167 rock powders were weighted in 15 ml Teflon vials. Immediately after, we added between 250
168 and 500 mg of ^{77}Se enriched spike and between 150 and 300 mg of ^{125}Te enriched spike. The
169 silicates were digested by adding successively 1 ml of 14M HNO_3 and 6 ml of 29M HF and
170 placing the vials on a hotplate at 90°C for 24 hours. The samples were evaporated at 70°C to
171 avoid major Se and Te volatilization (Vlastélic and Piro, 2022). The dry residues were taken in
172 3 ml of 6M HCl, heated at 90°C for 24H, and evaporated at 70°C. This step of HCl conversion
173 was repeated once. The two-step chemistry from Yierpan et al. (2018) was used to purify Se
174 and Te. The column separation was calibrated by dissolving 320 mg of a La Réunion basalt
175 doped with 500 ng of Se and Te. After HCl conversion, the sample residues were dissolved in
176 3 ml of 4M HCl, centrifuged for 5 min, before being loaded on anionic columns (polypropylene
177 Biorad filled with 5 ml of AG1-X8 100-200 mesh resin). Most elements and Se were eluted by
178 adding successively 3 x 1 ml and 4 ml of 4M HCl, while Te was retained probably as chloro-
179 complex. Iron was eluted with 2 x 5 ml of 2M HCl – 5M HF and 2 x 3 ml of 0.4M HCl. Tellurium,
180 with minor amount of remaining Pb, was eluted with 6 ml of 0.4M HCl. After evaporation at
181 65°C, the major element – Se fraction was dissolved in 4 ml of 0.1M HNO_3 and centrifugated
182 before being loaded on cationic columns (polypropylene Biorad filled with 5 ml of AG50-X8
183 200-400 mesh resin). Selenium was eluted by adding successively 2 x 1 and 3ml of 0.1M HNO_3 .
184 The collected Se fraction is not highly pure but is sufficiently depleted in Fe and other
185 transition metals for efficient hydride generation during subsequent ICPMS analysis.
186 After evaporation at 85°C the fractions of Se (0.14 – 135 ng) and Te (0.04 – 24 ng) recovered
187 from samples were taken in 6 and 3 ml of HNO_3 1M, respectively. The resulting solutions with
188 0.02- 23 ppb Se and 0.013 – 8 ppb Te were mixed online with 0.3 M NaBH_4 – 0.1 M NaOH in a
189 hydride generation system (HGX-200 from Teledyne Cetac Technologies). The H_2Te and H_2Se
190 vapors were entrained by two Ar flows (carrier flow of 0.42 L/min and make up flow of 0.82
191 L/min) to an Agilent 7500 ICPMS. To improve ICPMS sensitivity, we used two primary pumps
192 increasing the vacuum of the interface. $^{78}\text{Se}/^{77}\text{Se}$ was measured using the reaction cell (He

193 mode) to lower polyatomic interferences from the Ar carrier gas (e.g., $^{40}\text{Ar}^{38}\text{Ar}^+$, $^{36}\text{Ar}^{40}\text{Ar}^1\text{H}^+$,
 194 $^{38}\text{Ar}_2^1\text{H}^+$), while $^{126}\text{Te}/^{125}\text{Te}$ was measured in “no-gas” mode. Each measurement included
 195 typically 100 scans, with 200 ms acquisition on each mass, and lasted one minute. The 1M
 196 HNO_3 solution used to dissolve samples was repeatedly measured for background correction.
 197 Instrumental mass fractionation was corrected by measuring a 5 ppb Se isotopic standard
 198 (NIST SRM 3149) and a 1 ppb Te isotopic standard (NIST SRM 3156) at the beginning and/or
 199 at the end of each measurement session. Signals of ca. 130 000 CPS/ppb ^{78}Se and 500 000
 200 CPS/ppb ^{126}Te were measured on the NIST SRM solutions.

201 Sulfur concentration was measured by isotope dilution using a ^{34}S enriched spike (262 ppm S,
 202 with 99.79% ^{34}S). The spike, initially in the form of native sulfur, was dissolved in 14M HNO_3
 203 and calibrated against IAEA-S-1 sulfur isotope reference material. For sample analysis, 50 mg
 204 of rock powders were weighted in 15 ml Teflon vials, spiked and digested with 1 ml of 14M
 205 HNO_3 and 6 ml of 29M HF at 90°C for 24 hours. After evaporation, the fluoride residue was
 206 reduced by addition and evaporation of a few drops of 14M HNO_3 . Unlike Wang and Becker
 207 (2013) procedure, sulfur was not separated because of important S release (>1 μg) from the
 208 cationic resin. Instead, the residue was taken in 5 ml of H_2O , centrifugated, and the $^{32}\text{S}/^{34}\text{S}$
 209 ratio of the supernatant was directly analyzed on an Element XR ICP-MS in high mass-
 210 resolution mode ($m/\Delta m$ of 10 000). To check the accuracy of S isotope compositions, the
 211 $^{32}\text{S}/^{34}\text{S}$ ratios of a subset of samples from Fani Maoré volcano were also measured as oxides
 212 ($^{32}\text{S}^{16}\text{O}/^{34}\text{S}^{16}\text{O}$), using the oxygen reactive mode of an Agilent 8900 triple quadrupole ICPMS.
 213 Instrumental mass fractionation was corrected by running IAEA-S-1 sulfur isotope reference
 214 material. Sample concentration (C_{Sample}) was calculated according to Eq. 1 :

215

$$216 \quad C_{\text{Sample}} = C_{\text{Spike}} \times \frac{m_{\text{Spike}}}{m_{\text{Sample}}} \times \frac{Ab_{\text{Spike}}^{\text{B}}}{Ab_{\text{Sample}}^{\text{B}}} \times \frac{R_{\text{Spike}} - R_{\text{mes}}}{R_{\text{mes}} - R_{\text{Sample}}} \quad (1)$$

217

218 Where C_{Spike} is the spike concentration, m_{Spike} and m_{Sample} are the spike and sample masses,
 219 R_{Spike} , R_{Sample} and R_{mes} are the isotopic ratios of the spike, the sample and the measured
 220 sample-spike mixture, respectively. R_{Sample} being not measured, we use the natural
 221 abundances of Se and Te isotopes of the NIST standards. Ab^{B} is the isotopic abundance of the
 222 denominator isotope. The precision of isotopic ratios measured by ICPMS are on the order of

223 1-3 %. The precision of the concentrations obtained by isotope dilution is inferred from the
224 error magnification (M), defined as (Eq. 2) :

225

$$226 \quad M = \frac{\Delta C_{Sample}}{C_{Sample}} / \frac{\Delta R_{mes}}{R_{mes}} = \frac{R_{mes} \cdot (R_{Spike} - R_{Sample})}{(R_{Spike} - R_{mes}) \cdot (R_{mes} - R_{Sample})} \quad (2)$$

227

228 Error magnification ranges between 1.03 and 1.3 for most samples and reaches 2-3 for the
229 most depleted (olivine-rich basalt) or enriched (Réunion pumice and Pele's hairs) samples.
230 Average procedural blanks are 0.8 ng S, 0.2 ng Se and 0.05 ng Te. The concentrations of the
231 four reference basalts measured during this study (BHVO-2, BCR-2, BEN and BIR-1, Table 2)
232 fall within the range of the recommended values reported in the GeoRem database (Jochum
233 et al. 2005). However, our S value of BIR-1 (4.4 ppm) is much lower than the information value
234 of 70 ppm. La Réunion samples that were not previously analyzed for major and trace
235 elements were analyzed conventionally by ICP-AES (major elements) and ICPMS (trace
236 elements) using the methods described in Gurioli et al. (2018) and Vlastélic et al. (2013),
237 respectively. The only difference is that the plutonic rocks were dissolved using NH₄-HF₂
238 instead of HF-HNO₃ for ICPMS analysis to ensure complete dissolution.

239

240 5. Results

241

242 The concentrations of S, Se and Te of La Réunion and Fani Maoré samples are reported in
243 table 2. Major element and trace element data are reported in supplementary table S1.

244

245 5.1. S – Se – Te budget of La Reunion plutonic rocks

246

247 The Piton des Neiges wehrlites (SAL206 and CB150914) have 264 – 358 ppm S, 19 – 36 ppb Se
248 and 2.7 – 3.1 ppb Te. They show S/Se ratios (9985-16966) higher than La Réunion lavas and
249 mantle peridotites (S/Se < 8000) but preserve similar Se/Te ratios (6.1 – 13.2) (Fig. 3). The
250 Piton de la Fournaise wehrlite (CHI-7) has 12.7 ppm S, 9.96 ppb Se and 2.56 ppb Te and plot
251 within the compositional field of mantle peridotites (Fig. 3) (Lorand and Alard, 2010; Wang
252 and Becker, 2013). The S/Se (1275) and Se/Te (3.9) ratios of the CHI-7 sample are significantly
253 lower than in carbonaceous chondrites.

254

255 5.2. Differentiation of La Réunion and Mayotte magmas

256

257 Major and trace element variations during the differentiation of La Réunion and Mayotte
258 magmas are shown in [figure 4](#). The Réunion samples show four evolution steps, described in
259 [figure 4](#) caption, which are consistent with the sequence of low-pressure crystallization of La
260 Réunion magmas (e.g., Villemant et al. 2009; Pichavant et al. 2016). Compared to La Réunion
261 lavas, Fani Maoré lavas are characterized by lower Sc and V, in keeping with high-pressure
262 fractionation of clinopyroxene (Berthod et al., 2021) ([Fig. 4e,f](#)). Fani Maoré lavas also have
263 higher Th at given MgO ([Fig. 4h](#)).

264

265 5.3. Evolution of S, Se and Te in La Réunion magmas

266

267 La Réunion lavas are extensively depleted in sulfur (5 - 884 ppm S) compared to primitive
268 melts with up to 1800 ppm S (Bureau et al., 1998; Vigouroux et al., 2009; Di Muro et al., 2016)
269 ([Fig. 5a](#)). The least degassed submarine lavas from step 1 with 416 – 632 ppm S have already
270 lost between 65 and 77% S, while submarine lava from step 2 (119 – 146 ppm) have lost 92 %
271 of S mostly through degassing because the magmas are not yet sulfide saturated ([Fig. 5a](#)). In
272 subaerial conditions, lavas from step 1 (30 – 266 ppm S) have 36 to 95% less S than their
273 submarine counterpart, while lavas from steps 3 and 4 are even more depleted with 5 – 168
274 ppm S. Generally, sulfur concentration shows some scattering in subaerial lavas, and there is
275 only a rough trend of decreasing S with decreasing MgO.

276

277 In submarine environment, selenium displays a similar behavior as sulfur with relatively
278 uniform concentrations (74 – 131 ppb Se) in lavas from step 1 and lower concentrations (34 –
279 51 ppb Se) in lavas from step 2 ([Fig. 5b](#)). Unlike sulfur, the selenium contents of subaerial (121
280 \pm 21 ppb, n=10) and submarine lavas (104 \pm 16 ppb, n=8) from step 1 are similar. The absence
281 of subaerial degassing of Se results in a smooth trend of decreasing Se with decreasing MgO
282 in subaerial samples from Piton des Neiges, with less than 3 ppb Se in the most differentiated
283 samples ([Fig. 5b](#)). Most lavas fall within a narrow range of S/Se (2300 – 5000), close to the
284 chondritic value (2750 \pm 200), except for subaerial lavas with 4 – 8 wt% MgO where S/Se
285 decreases down to 400 due to degassing loss of S ([Fig. 5d](#)). The Cu/Se ratio is relatively uniform

286 (605 – 1234) in subaerial and submarine lavas from step 1, but markedly increases up to 3010
287 in the submarine lavas from stage 2 (Fig. 5e). This increase must reflect Se degassing because
288 Cu remains elevated during step 2 (Fig. 4d). The Cu/Se ratio then drops to 89 during step 3
289 and early step 4 due to sulfide saturation. During late step 4 (<2.5 wt% MgO), Cu/Se increases
290 again up to 9029 due to extensive Se degassing.

291

292 Tellurium shows more complex variations (Fig. 5c). The tellurium concentrations of submarine
293 lavas first decrease from 12.4 to 3.7 ppb as MgO decreases from 13 to 7.6 wt%, before
294 increasing abruptly until the end of step 1 (6 wt% MgO) where Te reaches 62 ppb. Then, Te
295 concentrations decrease again during stage 2, while remaining elevated (23 – 33 ppb).
296 Samples collected on land show a very different behavior, with a marked decrease of Te at
297 the end of step 1, from 2.95 to 0.38 ppb. Only sample SAL 51 seems to plot on the submarine
298 trends, possibly because this dyke sample emplaced under elevated pressure. An event of Te
299 increase above 1 ppb occurs during step 3, or early step 4, before the final decrease of Te
300 down to 0.2 ppb. The large variations of Se/Te (1 – 225) between 5 and 8 wt% MgO (Fig. 5f)
301 are mostly due to the large variations of Te between Te-depleted subaerial and Te-enriched
302 submarine lavas (Fig. 5c), while Se remains relatively uniform (Fig. 5b).

303

304 Noteworthy, a few samples with biased compositions plot outside the frame of Fig. 5 or are
305 highlighted: (1) The picritic sample (070408-1b) with 29.2% wt% MgO has low S (24 ppm), Se
306 (59 ppb) and Te (0.69 ppb) contents due to the occurrence of olivine crystals highly depleted
307 in S, Se and Te. Yet this sample has Se/Te (86) within the range of subaerial basalts. (2)
308 Compared to other subaerial samples with identical MgO content, the Pele's hairs sample
309 (200409-6) has 80 times more Te (120 ppb) and 5 times more Se (677 ppb), but similar S
310 concentration (196 ppm), yielding very low S/Se (290) and low Se/Te (5.7) ratios (Fig. 5 d,f).
311 (3) Some of the trachytes from Piton des Neiges (SAL 201 and SAL 203) hosting hydrothermal
312 pyrite have anomalously elevated S (730 – 884 ppm), and to a lesser extent Se (76 – 206 ppb)
313 and Te (1.3 – 2.5 ppb) contents. The occurrence of pyrite increases S/Se up to 9600 (Fig. 5d)
314 but does not seem to drastically fractionate the Se/Te ratios of these samples (58 – 83).

315

316 5.4. S – Se – Te signature of the 2018-2021 Fani Maoré submarine lavas

317

318 All Fani Maoré lavas are enriched in sulfur (1342 – 1711 ppm) compared to La Réunion lavas
319 (Fig. 5a), in agreement with the occurrence of droplets of iron sulfide (Berthod et al., 2021).
320 Within the narrow S range, we note a trend of increasing S concentration during the 2018-
321 2021 eruption with 1342 – 1413 ppm during phase 1 (July 2018 - May 2019), 1386 – 1509 ppm
322 during phase 2 (May 2019 - August 2019), and 1712 ppm during phase 3b (October 2020 -
323 January 2021). The S content (1430 ppm) of the magnesian sample DR11-0704 is consistent
324 with other samples produced during phase 2.

325 Unlike sulfur, the selenium concentration of Fani Maoré lavas (66 – 81 ppb) is only slightly
326 higher than La Réunion subaerial and submarine lavas (38 – 51 ppb) with similar MgO content,
327 excluding samples hosting pyrite (Fig. 5 b). Consequently, Fani Maoré lavas display very
328 elevated S/Se ratios (16929 – 22130) (Fig. 5 d), which increase slightly with decreasing MgO.
329 The tellurium concentrations (4.4 – 13.6 ppb) (Fig. 5 c), and Se/Te ratios (5.1 – 15.6) (Fig. 5 f)
330 of Fani Maoré lavas are within the range of La Réunion submarine lavas. The two most evolved
331 Fani Maoré samples (MgO <3.9 wt%) have distinctly higher Te contents (9.5 – 13.6 ppb) and
332 lower Se/Te ratios (5.1 – 7.2).

333

334 5.5. S – Se – Te degassing within the Fani Maoré pillow lava

335

336 The studied GFL-DR20-0101 pillow lava presents five concentric layers with distinctive
337 textures (Fig. 2): In the core of the pillow (layer 1), only rare small rounded (<1 mm) vesicles
338 occur. The overlying thick layer 2 shows the occurrence of 1-3 cm pipe vesicles with radial
339 distribution. The number of pipes markedly increases in layer 3. However, closer to the surface
340 where the extent of crystallization decreases, neither vesicles nor degassing pipes occur in
341 layers 4, 5 and 6. Layer 5 stands out from layer 4 due to the occurrence of glass, while the
342 pillow rim (layer 6) is fully glassy. This textural structure is very similar to that described by
343 Berthod et al. (2022) for a pillow lava erupted earlier during the eruption. More generally, this
344 degassing-crystallization structure is typical of pillows lavas (e.g., Philpotts and Lewis, 1987;
345 Merle et al., 2005).

346 Variations of S, Se and Te concentrations, and S/Se and Se/Te ratios from pillow rim to pillow
347 core are reported in figure 6. Sulfur and Se display similar variations, with the base of layer 2
348 being depleted in S (1518 – 1593 ppm) and Se (76.8 – 77.0 ppb) compared to pillow core (1671
349 – 1794 ppm S and 82.6 – 83.5 ppb Se) and external layers (1751 – 1881 ppm S and 82.1 – 83.6

350 ppb Se). Sulfur loss (13%) being more important than Se loss (7%), S/Se is lower in layer 2
351 (19706 – 20738) compared to pillow core (20235 – 21496) and external layers (21243 –
352 22641). Tellurium displays a different zonation pattern, with low and homogeneous
353 concentrations (4.5 – 4.9 ppb) in the internal layers 1 and 2, and markedly higher
354 concentrations (5.7 – 6.0 ppb) in the external layers 3-6. Consequently, the Se/Te ratio is lower
355 in the external layers (13.8 – 14.7) compared to the internal layers (16.3 – 17.2). Concentration
356 profiles are also reported for elements showing remarkable variations across the pillow. Like
357 S and Se, Mo and W are markedly depleted (20 – 30%) in the intermediate layer 2 compared
358 to pillow core and rim. Unlike lighter alkali, Cs is also depleted (12%) in the outer part of layer
359 2. Antimony is enriched in the outermost layer of the pillow.

360

361 6. Discussion

362

363 6.1. Processes controlling selenium retention in and degassing from magmas

364

365 The drop of sulfur solubility in oxidized melts below 100 MPa (Lesne et al., 2011; Di Muro et
366 al., 2016) explains why sulfur outgassing from submarine lavas generally increases with
367 decreasing water depth and is extensive in shallow or subaerial lavas. No experimental work
368 has characterized selenium degassing during magma decompression, but several studies of
369 oceanic basalts noted that, unlike sulfur, selenium is retained in seafloor lavas emplaced over
370 a wide depth range (Jenner et al., 2010; Lissner et al., 2014; Yierpan et al. 2019, 2021; Kurzawa
371 et al., 2019). This work shows that moderately differentiated ($\text{MgO} > 6\%$) subaerial lavas from
372 La Réunion Island also preserve the same Se content as their submarine counterpart (Fig. 5b),
373 while S is extensively lost (Fig. 5a). Jenner et al. (2010) suggested that selenium must be
374 stabilized in silicate melts as Se^{2-} , in the same manner as sulfur is stabilized as S^{2-} . The
375 stabilization mechanism involves substitution of S^{2-} and Se^{2-} for O^{2-} in the silicate liquid (Wykes
376 et al., 2015). The low volatility of Se during final magma ascent and decompression may be
377 related to the selenide-selenate transition occurring at an oxygen activity $> 10^3$ higher than
378 the sulfide-sulfate transition. In the relatively oxidized redox conditions of undegassed basaltic
379 magmas (near the nickel nickel-oxide buffer, Moussallam et al. 2016; Pichavant et al., 2016) a
380 large fraction of sulfur occurs as sulfate not stabilized in the silicate melt and thus available
381 for degassing, while selenium still occurs as selenides retained in the silicate melt structure.

382 During magma differentiation, Se loss starts during step 2, where clinopyroxene and
383 plagioclase join olivine as major fractionating phases, and is extensive during step 4 where
384 sulfide is stable (Fig. 5). This can be explained either by (1) Se degassing and/or (2) the
385 fractionation of a sulfide phase in which Se partition. Note that selenide saturation has hardly
386 any chance to form because Selenium Content at Selenide Saturation ($\text{SeCSes} > 1000$ ppm) is
387 much higher than the total Se budget of magmas ($\text{Se} < 0.5$ ppm) (Wykes et al., 2015). The drop
388 of Se concentration in the most differentiated subaerial lavas from La Réunion Island ($\text{Se} < 5$
389 ppb for $\text{MgO} < 2$ wt%) contrasts with the subtle Se decrease reported for evolved submarine
390 lavas from convergent margins (Jenner et al., 2015; Kurzawa et al. 2019), where Se remains
391 above 70 ppb even in the most evolved samples. For La Réunion samples, the drop of Se below
392 4 wt% MgO correlates with a factor of 100 increase of Cu/Se (Fig. 5), from 89 to 9020. Selenium
393 being more volatile than Cu, but less compatible in sulfide, the Cu/Se ratio reflects the
394 contribution of Se degassing (high Cu/Se) relative to sulfide saturation (low Cu/Se). This
395 observation indicates that Se exhaustion in the most evolved lavas from La Réunion results
396 from extensive degassing, either during shallow magma storage or during eruption.

397
398 The question then arises as to how and why Se volatilizes during magma differentiation, while
399 it does not during magma decompression. The critical decrease of Se between 6.0 and 0.5%wt
400 MgO (Fig. 5b) despite the important decrease of the melt fraction (a factor of 6 based on Th
401 increase, Fig. 4h) requires a major drop of Se solubility. Selenium must remain in the form of
402 Se^{2-} in a differentiating melt that becomes increasingly reduced due to SO_2 degassing
403 (Moussallam et al. 2016). If Se^{2-} substitutes for O^{2-} in the melt, it is hypothesized that the Se—
404 (Si, Al) bonds are weaker than the original O—(Si, Al) bonds and are preferentially broken
405 during crystal nucleation and growth, releasing Se. Kinetic might also play a major role
406 because magma storage and differentiation occur over long timescales compared to magma
407 ascent, which inevitably facilitates the diffusion and loss of volatile elements. For instance, it
408 took about 300 ka for Piton des Neiges olivine basalts to evolve into trachyte (Upton and
409 Wadsworth, 1972; Gillot and Nativel, 1982), whereas Piton de la Fournaise magmas can
410 ascend from crustal reservoirs to the surface in a matter of days (Battaglia et al., 2005).
411 Between these two end-member cases, variable Se loss is expected in the current steady-state
412 regime of Piton de la Fournaise, where magmas undergo static degassing during their storage
413 at different depths before being rapidly extruded. Interestingly, S/Se is little fractionated in

414 the most differentiated subaerial lavas ($\text{MgO} < 4 \text{ wt\%}$). This suggests that in the reducing
415 conditions of differentiated magmas, sulfur dominantly occurs as S^{2-} and follows the same
416 degassing processes as Se. However, detailed inspection of the data (Fig. 5) reveals a slight
417 decrease of S/Se in the most differentiated samples (step 4), in keeping with the high S/Se of
418 cumulative rocks (Fig. 3) where sulfides accumulate (Upton et al., 2000).

419

420 6.2. Tellurium specific behavior

421

422 As for sulfur, tellurium is extensively lost from subaerial lava, with nearly no overlap between
423 Te-depleted subaerial lavas and Te-enriched submarine lavas: in the Réunion-Mayotte data
424 set, 18 out of the 20 subaerial samples have less than 3.5 ppb Te, whereas all the submarine
425 lavas (20) have more than 3.5 ppb Te. This feature is also generally seen in the global OIB data
426 set (Yi, 2000; Forrest et al., 2017, Yierpan et al., 2021), although some well-documented
427 subaerial basalts from Hawaii (BHVO2 from Kilauea with 14.2 ppb Te) or Iceland (BIR-1 from
428 Iceland with 5.8 ppb Te) have similar Te content as their submarine counterparts (Yierpan et
429 al., 2018). Like S and Se, Te^{2-} solubilizes in silicate melt by replacing O^{2-} (Renggli et al, 2022).
430 The telluride – tellurate transition occurring at similar oxygen fugacity as the sulfide – sulfate
431 transition (McPhail et al., 1995), only a fraction of Te occurs as soluble Te^{2-} in the redox
432 conditions of basaltic magmas. Tellurium exsolution and volatilization at atmospheric
433 pressure might thus result from partial oxidation, as for sulfur.

434 During the crystallization sequence of La Réunion magmas, major degassing-induced loss of
435 Te (from 2.9 to 0.38 ppb) occurs in subaerial lavas between MgO of 8.2 and 5 wt%.
436 Remarkably, over the same MgO range where Te is extensively lost from subaerial lavas, the
437 Te content of submarine lavas rises from 3.7 to 62 ppb Te, exceeding the highest
438 concentrations reported so far in submarine basalts (29.2 ppb Te in one sample from Loihi
439 seamount, Hawaii, Yi et al., 2000). Such enrichment cannot be explained by crystallization
440 alone because the concentration of highly incompatible elements, like Th, increases by no
441 more than 50%. Another possibility is that the most elevated Te concentrations of submarine
442 basalts result from sample contamination with seawater derived Fe-Mn oxides, in which Te is
443 enriched more than any other elements relative to Earth crust (Hein et al., 2003). However,
444 we consider this possibility as unlikely because (i) the whole rock powders analyzed were
445 made from the interior of the pillow lavas (Smietana, 2011), and (ii) elements highly enriched

446 in Fe-Mn crusts, such as Mn and Co, do not show anomalous concentrations in the Te-enriched
447 samples. Instead, the anomalous Te increase correlates with a marked increases of the
448 metalloids As (from 1 to 13.8 ppm) and Sb (from 0.1 to 1 ppm), suggesting that Te is mobilized
449 and enriched by degassing processes. We also note that, despite very different volcanic and
450 petrologic contexts, Te concentration also anomalously increases in the most differentiated
451 lavas from the Fani Maoré eruption (Fig. 5c), hence pointing to a general process. We
452 hypothesize that Te enrichment at some steps of magma evolution could result from Te
453 exsolution from deep melts, transfer and accumulation in magmas stored at shallower depth,
454 in a similar manner as CO₂ fluxing (Blundy et al., 2010). Such process is supported by the lower
455 solubility of Te in silicate melts compared to S and Se (Helmy et al., 2020). Alternatively, Te
456 accumulation could occur after eruption at the surface of thick lavas flows that undergo
457 internal differentiation and degassing, in a similar manner as Li, B and Cs (Kuritani and
458 Nakamura, 2006). In this second hypothesis, Te enrichment of some submarine samples
459 would result from the preferential sampling of the surface of submarine lava flows during
460 dredging. In both cases, extensive degassing of Te in subaerial setting is expected to prevent
461 Te accumulation in the lavas.

462

463 6.3. Assessment of S – Se – Te degassing during the emplacement of Fani Maoré submarine
464 lavas

465

466 Pillow lava degassing is a complex process due to the opposite effects of rim quenching and
467 progressive cooling and crystallization of pillow interior. Previous studies reported differences
468 in S, Se and Te concentrations between pillow interiors and glassy rims (Lissner 2014; Forrest
469 et al. 2017). They noted that sulfur concentration is generally lower in pillow interiors, and
470 that the difference between rim and interior is less systematic for Se, and especially for Te.
471 The compositional profile reported here for a sample from the Fani Maoré eruption provides
472 a more detailed view on pillow degassing, revealing that only the intermediate layer of the
473 pillow hosting pipes vesicles is extensively outgassed in S and Se. Pipes vesicles are the textural
474 remnants of the internal degassing of pillow lavas. They are thought to form by exsolution of
475 gas from crystallizing magma onto bubbles attached to the advancing solidification front
476 (Philpotts and Lewis, 1987). Merle et al. (2005) estimated that at least 25 vol% crystallization
477 is necessary to produce a crystal framework required for generating the segregation

478 structures in pillows. In the studied differentiated Fani Maoré sample (MgO of 4.45 wt%), pipe
479 vesicles are not rooted deep in the pillow, which explains the degassing of the intermediate
480 layer mainly. Unlike S and Se, Te is depleted in both layers 1 and 2, showing a zonation (Fig. 6)
481 unrelated to the pipe vesicles. This suggests that Te does not behave as major volatile
482 species. To explain Te degassing of layer 1 in the absence of degassing pipes, it is hypothesized
483 that Te is less soluble than major volatile species in silicate melts and is lost earlier by diffusion.
484 In support of this possibility, Te is less soluble than S and Se in silicate melts saturated in
485 sulfide, selenide and telluride (Helmy et al., 2020).

486 The compositional profile reported on figure 6 allows an assessment of pillow degassing
487 during emplacement and cooling. The sample was divided into nine shells (s) corresponding
488 to the nine analyzes. The boundary between each shell was set at equal distance between
489 neighboring drill holes (Fig. 2). The volume of each shell (V_s) was calculated assuming a
490 spherical geometry. The density (ρ) of the pillow was assumed to be uniform ($\rho_s = \rho_{tot}$). At the
491 scale of the pillow, the mass fraction of element lost by degassing (ϵ) is calculated according
492 to (Eq. 3):

493

$$494 \quad \epsilon_x = 1 - \frac{\sum_{s=1}^{s=9} [X]_s \times V_s \times \rho_s}{[X]_{max} \times V_{tot} \times \rho_{tot}}$$

495

496 Where $[X]_s$ is the element concentration in shell s, and $[X]_{max}$ is the highest concentration
497 measured in the pillow thought to be close to the pre-eruptive value. Values of ϵ are 6.5% for
498 S, 7.2% for Te, but only 1.6% for Se confirming the lower volatility of Se during lava
499 emplacement. Chalcogens degassing is accompanied with significant loss of W ($\epsilon = 8.9\%$), Mo
500 ($\epsilon = 5.1\%$) and Cs ($\epsilon = 5.1\%$), which appear to be much more volatile than during subaerial
501 eruptions where ϵ is lower than 0.15% for those three elements (Rubin et al., 1997). W and
502 Mo are highly refractory elements, but their oxides are known to volatilize readily at 1000°C
503 and 1 atmosphere pressure in the presence of water vapor (Millner and Neugebauer, 1949),
504 and this effect is expected to increase with pressure. Thus, water exsolution from the pillow
505 seems to have played a role in mobilizing refractory elements. Between 2018 and 2021, the
506 Fani Maoré submarine eruption produced 6.5 km³ of lava with an average vesicularity of 27%
507 (i.e., 4.8 km³ of dense rock) (Berthod et al., 2021). Using a dense rock density of 2500 kg/m³
508 (Verdurme et al., 2024) and the highest element concentrations of the three eruptive phases

509 as reference, it is estimated from the ϵ values that the Fani Maoré eruption released 1.1 – 1.5
510 $\times 10^6$ tons of S, 2300 – 2700 tons of Mo, 970 – 1130 tons of W, 194 – 339 tons of Cs, 13.3 – 16
511 tons of Se and 4.5 – 11.8 tons of Te. By comparison the Se amount released in the ocean by
512 the Fani Maoré eruption corresponds to 1% of the annual degassing flux of mid-ocean ridges
513 (Rubin et al., 1997).

514

515 6.4. Brief constraints on magma sources

516

517 The elevated S/Se ratios of the two Piton des Neiges wehrlites confirm previous field and
518 petrological inferences (Berthod et al., 2020) that the samples formed at the bottom of a
519 magma chamber where they accumulated dense sulfides (Fig. 3). Conversely, the S – Se – Te
520 signature of Piton de la Fournaise wehrlite (CHI-7) is consistent with a mantle origin. Its low
521 S/Se and Se/Te ratios relative to the Bulk Silicate Earth (BSE) (Fig. 3), together with its
522 depletion in incompatible elements (Table S1), indicate that this sample is a mantle residue
523 after melt extraction. To reconstruct the possible composition of the parental fertile
524 peridotite, the CHI-7 melting residue is mixed with the extracted melts, best represented by
525 the erupted lavas. The resulting mixing curve intercept the BSE composition (Fig. 3), raising
526 the possibility that the La Réunion plume source preserved the same S/Se and Se/Te ratios as
527 the BSE and CI chondrites. This agrees with previous inferences from Highly Siderophile
528 Elements (Peters et al., 2016) and U-Th-Pb isotope systematics (Vlastélic et al., 2006) that the
529 Réunion plume samples a less differentiated mantle domain.

530 All Fani Maoré lavas including the magnesian sample (MAY04-DR11-0704) display S/Se ratios
531 (16929 – 22130) that are much higher than in worldwide MORB and OIB ($S/Se < 10000$). The
532 S/Se ratios of Fani Maoré lavas are also higher than the most fertile mantle peridotites
533 ($S/Se \sim 8000$) (Wang and Becker, 2013) and the cumulative rocks from La Réunion (10000
534 $< S/Se < 14000$, Fig. 3), which are known to be enriched in sinking sulfur liquids (Upton et al.,
535 2000). Fani Maoré's S – Se signature is hardly explained by magma generation processes and
536 must reflect a source property. The most likely explanation is that the Fani Maoré lavas derive
537 from the melting of a lithospheric mantle extensively refertilized by sulfide melts. This is
538 consistent with previous inferences that the Fani Maoré volcano, like the island of Mayotte,
539 formed by melting of a carbonated mantle source enriched in Ba and volatiles (Chauvel et al.
540 2024; Pelleter et al. 2014). Lithosphere refertilization is a common process driven by melt or

541 fluid infiltrations, but in the case of the Fani Maoré volcano, it might have reached an unusual
542 extent and caused this exceptionally large-volume eruption.

543

544 7. Conclusions

545

546 This work obtained the following results:

547 (1) Unlike sulfur, selenium degassing is not significant during the final (30 – 0.1 MPa),
548 presumably rapid ascent of moderately differentiated (MgO > 6wt%) magmas from La
549 Réunion. Conversely, selenium degassing occurs during magma differentiation below 6 wt%
550 MgO, at a similar rate as sulfur, yielding small S/Se fractionation in the residual magma. The
551 long timescales require to markedly differentiate La Réunion magmas certainly facilitates the
552 diffusion and loss of less volatile selenium. Variable Se loss is expected in the intermediate
553 situations involving both static degassing during magma storage and crystallization followed
554 by rapid extrusion of magma.

555 (2) During the evolution of La Réunion magma reservoir, the onset of sulfide saturation occurs
556 between ~5 and ~4 wt% MgO, while olivine just left the liquidus, and Ti-magnetite has not yet
557 appeared. Sulfide fractionation controls Cu/Se variations over this narrow MgO range, while
558 degassing dominates outside.

559 (3) As sulfur, tellurium is extensively lost from La Réunion subaerial lavas, whereas submarine
560 lavas tend to retain Te and possibility accumulate Te near 6% MgO. The contrasted behavior
561 of Se and Te yields extremely large Se/Te variations between subaerial (up to 225) and
562 submarine (down to 1.0) lavas.

563 (4) A pillow lava emplaced during the Fani Maoré eruption offshore Mayotte shows degassing-
564 driven radial compositional zonation. Degassing of S, Se and other moderately volatile
565 elements (Mo, W, Cs) is the most important at intermediate depth within the pillow where
566 pipe vesicle occur, suggesting they escape with major volatiles. Conversely, Te is depleted in
567 the whole interior of the pillow, suggesting Te is more efficiently lost due to a lower solubility
568 in magma.

569 (5) Assessment of pillow degassing during emplacement yields losses of 6.5% for S, 7.2% for
570 Te, but only 1.6% for Se confirming the lower volatility of Se during lava emplacement.
571 Chalcogens degassing is accompanied with significant loss of W (8.9%), Mo (5.1%) and Cs
572 (5.1%). Based on these values, the 6.5 km³ Fani Maoré eruption released 1.1 – 1.5 x 10⁶ tons

573 of S, 2300 – 2700 tons of Mo, 970 – 1130 tons of W, 194 – 339 tons of Cs, 13.3 – 16 tons of Se
574 and 4.5 – 11.8 tons of Te during emplacement.

575 (6) The reconstructed S – Se – Te composition of La Réunion plume source is consistent with
576 the preservation of chondritic S/Se and Se/Te ratios, in agreement with previous suggestions
577 that the Réunion plume samples a less differentiated mantle domain.

578 (7) The unusually elevated S/Se ratios (16929 – 22130) of Fani Maoré lavas suggests that the
579 mantle source of this exceptional eruption has been extensively fertilized by sulfide melts.

580

581 **Acknowledgements**

582

583 Se and Te NIST Standard Reference Materials were obtained from S. König, and ³⁴S-enriched
584 spike from P. Cartigny. We are grateful to Captain, Officers, and crew members of the
585 GEOFLAMME oceanographic cruise (CNFH; PI C. Cathalot, E. Rinnert, N. Feuillet,
586 <https://doi.org/10.17600/18001297>) onboard the R/V Pourquoi Pas? (GENAVIR/IFREMER,
587 SHOM). The GEOFLAMME oceanographic funded marine operations that benefited to this
588 study and provided dredged samples.

589

590 **Figure captions**

591

592 Figure 1. Location maps. (a) Relief map of the southwest Indian Ocean showing the locations
593 of La Réunion and Mayotte islands. (b) Relief map of La Réunion Island showing the location
594 of the Piton des Neiges and Piton de la Fournaise volcanoes, and the location of subaerial and
595 submarine samples analyzed in this study. Closed triangles: Piton des Neiges lavas; closed
596 circles: Piton de la Fournaise lavas; closed hexagons: cumulates ; closed diamond: peridotite,
597 open circles: submarine lavas. (c) Relief map of Mayotte Island, showing the locations of the
598 samples from the Fani Maoré submarine eruption (open diamonds) that occurred between
599 2018 and 2021 50 km east of Mayotte island, along the East-Mayotte submarine Volcanic
600 Chain. All maps were made using GeoMapApp (<https://www.geomapapp.org/>).

601

602 Figure 2. Cross section of GFL-DR20-0101 pillow lava emplaced during phase 3 of the Fani
603 Maoré eruption. Drill holes are shown and numbered from pillow interior (DR20-1) to pillow
604 rim (DR20-12). Sample DR20-Sp is a chip taken from the thin glassy layer at the surface of the
605 pillow. The five main textural unit (1-5) and the surface glassy layer (layer 6) described in text
606 are indicated. Because the external layers 4 and 5 are thinner than other layers, between 3
607 and 4 smaller drill holes were made and mixed within each layer.

608

609 Figure 3. Composition of La Réunion plutonic rocks reported in (a) S/Se and (b) Se/Te versus
610 Al_2O_3 plots. The compositional field of mantle peridotites, and the composition of
611 carbonaceous chondrites (CI) and Bulk Silicate Earth (BSE) are shown (Lorand and Alard, 2010;
612 König et al., 2012; Wang and Becker, 2013). Closed hexagons: cumulates; closed diamond:
613 peridotite. Analytical error is smaller than symbols size. Data are from [table 2](#) (S, Se and Te
614 concentrations) and supplementary [table S1](#) (Al_2O_3 concentrations). The dashed line is a
615 mixing curve calculated by mixing CHI-7 peridotite with the less degassed submarine DR6-2
616 lava sample.

617

618 Figure 4. Major-trace elements versus MgO plot showing the composition of La Réunion and
619 Fani Maoré lavas. Vertical thin lines indicate major changes in the crystallization assemblage.
620 The crystallization sequences of La Réunion magma involves four steps (Villemant et al. 2009;
621 Pichavant et al. 2016) : (1) primary melts ($MgO \geq 9\%$) first crystallize olivine and spinel causing

622 an important decrease of Ni and Cr; (2) Clinopyroxene and plagioclase appear at the liquidus
623 at MgO~6 wt% as recorded by the onset of Sc, V and Ca/Al decrease. (3) Between ~5 and ~4
624 wt% MgO, the increase of Fe and Ti indicate that olivine is no longer a liquidus phase, while
625 Ti-magnetite has not yet appeared. The abrupt drop of Cu (from 97 to 18 ppm) indicates that
626 the onset of sulfide saturation occurs at this step. This corresponds to the first phase of sulfide
627 formation which is triggered by S becoming saturated in magmas (Collins et al. 2012). (4)
628 Below ~4 wt% MgO, the decrease of Fe, Ti, Ca/Al, Sc and Cu, and the increase of Th are
629 consistent with precipitation of clinopyroxene, plagioclase, magnetite and sulfides. This
630 second phase of sulfide saturation is related to the crystallization of titanomagnetite which
631 reduces the sulfur content at sulfide melt saturation (Jenner et al., 2010; Collins et al. 2012).
632 The crystallization assemblage of Fani Maoré samples (80% Cpx – 20 % Ol) is from Berthod et
633 al. (2021). Symbols are as in previous figures. Data are from [table 2](#) (S, Se and Te
634 concentrations) and supplementary [table S1](#) (major and trace element concentrations from
635 La Réunion samples). Fani Maoré data are from Berthod et al. (2022) (major elements) and
636 Chauvel et al. (2024) (trace elements). Fani Maoré trace element data not given in Chauvel et
637 al. (2024) were taken from Berthod et al. (2022).

638
639 Figure 5. Chalcogen contents (S, Se, Te) and ratios (S/Se, Cu/Se, Se/Te) plotted against MgO
640 content of lavas. Vertical thin lines indicate major changes in the mineral assemblage
641 crystallizing (see figure 4). The composition of La Réunion and Fani Maoré lavas are reported
642 using the same symbols as in previous figures. Analytical error is smaller than symbols size.
643 Data are from [table 2](#) (S, Se and Te concentrations) and supplementary [table S1](#) (MgO and Cu
644 concentrations from La Réunion samples). Fani Maoré data are from Chauvel et al. (2024) (Cu)
645 and Berthod et al. (2022) (MgO and Cu).

646
647 Figure 6.
648 Radial compositional zonation of GFL-DR20-0101 pillow lava emplaced during the third and
649 last phase (October 2020 - January 2021) of the Fani Maoré eruption (Berthod et al., 2020).
650 Vertical dashed lines separate the major textural units shown in [figure 2](#) and described in text.
651 Error bars are indicated or smaller than symbols size. Data are from [table 2](#) and supplementary
652 [table S1](#).

653 **References**

654

655 Albarède, F., Luais, B., Fitton, G., Semet, M., Kaminski, E., Upton, B. G. J., Bachèlery, P.,
656 Cheminée, J. L., 1997. The geochemical regimes of Piton de la Fournaise volcano
657 (Réunion) during the last 530 000 years. *J. Petrol.* 38, 171–201.

658 Battaglia, J., Ferrazzini, V., Staudacher, T., Aki, K., Cheminée, J.-L., 2005. Pre-eruptive migration
659 of earthquakes at the Piton de la Fournaise volcano (Réunion Island). *Geophys. J. Int.*
660 161, 549–558.

661 Barrat J.-A., Bachèlery Patrick, 2019. La Réunion Island dunites as analogs of the Martian
662 chassignites: Tracking trapped melts with incompatible trace elements. *Lithos* 344–
663 345, 452-463.

664 Berthod, C., Michon, L., Famin, V., Welsch, B., Bachèlery, P., Bascou, J., 2020. Layered gabbros
665 and peridotites from Piton des Neiges volcano, La Réunion Island. *J. Volcanol.*
666 *Geotherm. Res.* 405, 107039.

667 Berthod, C., et al., 2021. The 2018-ongoing Mayotte submarine eruption: Magma migration
668 imaged by petrological monitoring. *Earth Planet. Sci. Lett.* 571, 117085.

669 Berthod, C., et al., 2022. Temporal magmatic evolution of the Fani Maoré submarine eruption
670 50 km east of Mayotte revealed by in situ sampling and petrological monitoring.
671 *Collect. C. R. Geosci.* 354 (S2), 195–223.

672 Blundy, J., Cashman, K.V., Rust, A., Witham, F., 2010. A case for CO₂-rich arc magmas. *Earth*
673 *Planet. Sci. Lett.* 290, 289-301.

674 Bonneville, A., Barriot, J.P., Bayer, R., 1988. Evidence from geoid data of a hotspot origin for
675 the southern Mascarene Plateau and Mascarene Islands, (Indian Ocean). *J Geophys*
676 *Res* 93, 4199–4212.

677 Bureau, H., Pineau, F., Métrich, N., Semet, M.P., Javoy, M., 1998. A melt and fluid inclusion
678 study of the gas phase at Piton de la Fournaise volcano (Reunion Island). *Chem. Geol.*
679 147, 115-130.

680 Chauvel, C., Inglis, E. C., Gutierrez, P., Luu, T.-H., Burckel, P., Besson, P., 2024. Fani Maoré, a
681 new “young HIMU” volcano with extreme geochemistry, *Earth Planet. Sci. Lett.* 626,
682 118529.

683 Class, C., Goldstein, S., Stute, M., Kurz, M., Schlosser, P., 2005. Grand Comore Island: A well-
684 constrained “low 3He/4He” mantle plume. *Earth Planet. Sci. Lett.* 233, 391–409.

685 Collins, S.J., Maclennan, J., Pyle, D.M., Barnes, S.J., Upton, B.G.J., 2012. Two phases of sulphide
686 saturation in Reunion magma: evidence from cumulates. *Earth Planet. Sci. Lett.* 337–
687 338, 104–113.

688 Deniel, C., Kieffer, G., Lecointre, J., 1992. New ²³⁰Th–²³⁸U and ¹⁴C age determinations from
689 Piton des Neiges volcano, Reunion—A revised chronology for the Differentiated Series.
690 *J. Volcanol. Geotherm. Res.* 51, 253–267.

691 Di Muro, A., Métrich, N., Allard, P., Aiuppa, A., Burton, M., Galle, B., 2016. Magma degassing
692 at Piton de la Fournaise Volcano. In: *Active Volcanoes of the Southwest Indian Ocean*.
693 Springer, Berlin, Heidelberg, pp.203–222.

694 Edmonds M., Mather T.A., Liu E.J., 2018. A distinct metal fingerprint in arc volcanic emissions.
695 *Nat. Geosci.* 11, 790–794.

696 Emerick, C.M., Duncan, R.A., 1982. Age progressive volcanism in the Comores Archipelago,
697 western Indian Ocean and implications for Somali plate tectonics. *Earth Planet. Sci.*
698 *Lett.* 60, 415–428.

699 Famin, V., C. Berthod, L. Michon, J. Eycheenne, E. Brothelande, M.-M. Mahabot, M. Chaput,
700 2016. Localization of magma injections, hydrothermal alteration, and deformation in a
701 volcanic detachment (Piton des Neiges, La Réunion). *J. Geodynamics* 101, 155-169.

702 Famin, V., Michon, L., Bourhane, A., 2020. The Comoros archipelago: a right-lateral transform
703 boundary between the Somalia and Lwandle plates. *Tectonophysics* 789, 228539.

704 Famin, V., C. Paquez, M. Danišík, N. J. Gardiner, L. Michon, C. K. Kirkland, C. Berthod, B.
705 Friedrichs, A. K. Schmitt, P. Monié, 2022. Multi-technique Geochronology of Intrusive
706 and Explosive Activity on Piton des Neiges Volcano, Réunion Island. *Geochem.*
707 *Geophys. Geosyst.* 23, e2021GC010214.

708 Feuillet, N., Jorry, S., Crawford, W.C., Deplus, C., Thinson, I., Jacques, E., Saurel, J.M., Lemoine,
709 A., Paquet, F., Satriano, C., Aiken, C., Foix, O., Kowalski, P., Laurent, A., Rinnert, E.,
710 Cathalot, C., Donval, J.-P., Guyader, V., Gaillot, A., Scalabrin, C., Moreira, M., Peltier, A.,
711 Beauducel, F., Grandin, R., Ballu, V., Daniel, R., Pelleau, P., Gomez, J., Besançon, S., Geli,
712 L., Bernard, P., Bachelery, P., Fouquet, Y., Bertil, D., Lemarchand, A., Van der Woerd,
713 J., 2021. Birth of a large volcanic edifice offshore Mayotte via lithosphere-scale dyke
714 intrusion. *Nat. Geosci.* 14, 787–795.

715 Forrest, A., Kelley K.A., Schilling J.G., 2017. Selenium, tellurium and sulfur variations in basalts
716 along the Reykjanes Ridge and extension over Iceland, from 50°N to 65°N.
717 Interdisciplinary Earth Data Alliance (IEDA). doi: 10.1594/IEDA/100700.

718 Gillot, P.-Y., Nativel, P., 1982. K-Ar chronology of the ultimate activity of Piton des Neiges
719 volcano, Reunion Island, Indian Ocean. *J. Volcanol. Geotherm. Res.* 13, 131–146.

720 Gillot, P.-Y., Nativel, P.-E., 1989. Eruptive history of the Piton de la Fournaise volcano, Réunion
721 Island, Indian Ocean. *J. Volcanol. Geotherm. Res.* 36, 53–65.

722 Gurioli, L., Di Muro, A., Vlastélic, I., Moune, S., Villeneuve, N., Bachèlery, P., Valer, M., Thivet,
723 S., Boudoire, G., Peltier, A., Ferrazzini, V., Métrich, N., Benbakkar, M., Cluzel, N.,
724 Constantin, C., Devidal, J.-L., Fonquernie, C., Hénot, J.-M., 2018. Integrating field,
725 textural and geochemical monitoring to track eruption triggers and dynamics: a case-
726 study from Piton de la Fournaise. *Solid Earth*, 9, 431–455.

727 Greenland, L.P., Aruscavage, P., 1986. Volcanic emission of Se, Te, and As from Kilauea
728 volcano, Hawaii. *J. Volcanol. Geotherm. Res.* 27, 195-201.

729 Hajash, A., Armstrong, R.L., 1972. Paleomagnetic and radiometric evidence for the age of the
730 Comores Islands, west central Indian Ocean. *Earth Planet. Sci. Lett.* 16, 231–236.

731 Hein, J.R., Koschinsky A., Halliday A.N., 2003. Global occurrence of tellurium-rich
732 ferromanganese crusts and a model for the enrichment of tellurium. *Geochim.*
733 *Cosmochim. Acta* 67, 1117–1127.

734 Helmy, H.M., Ballhaus, C., Fonseca, R.O.C., Leitzke, F.P., 2020. Concentrations of Pt, Pd, S, As,
735 Se and Te in silicate melts at sulfide, arsenide, selenide and telluride saturation:
736 evidence of PGE complexing in silicate melts? *Contrib. Mineral. Petrol.* 175, 65.

737 Hertogen, J., Janssens, M.-J., Palme, H., 1980. Trace elements in ocean ridge basalt glasses:
738 implications for fractionations during mantle evolution and petrogenesis. *Geochim.*
739 *Cosmochim. Acta* 44, 2125-2143.

740 Jenner, F.E., Hauri, E.H., Bullock, E.S., König, S., Arculus, R. J., Mavrogenes, J. A., Mikkelsen, N.,
741 Goddard, C., 2015. The competing effects of sulfide saturation versus degassing on the
742 behavior of the chalcophile elements during the differentiation of hydrous melts,
743 *Geochem. Geophys. Geosyst.*, 16, 1490–1507, doi:10.1002/2014GC005670.

744 Jochum, K.P., Nohl, U., Herwig, K., Lammel, E., Stoll, B., Hofmann A.W., 2005. GeoReM: A New
745 Geochemical Database for Reference Materials and Isotopic Standards. *Geostand.*
746 *Geoanal. Res.* 29, 333-338.

747 König, S., Luguët, A., Lorand, J.-P., Wombacher, F., Lissner, M., 2012. Selenium and tellurium
748 systematics of the Earth's mantle from high precision analyses of ultradepleted
749 orogenic peridotites. *Geochim. Cosmochim. Acta* 86, 354–366.

750 Kuritani, T., Nakamura, E., 2006. Elemental fractionation in lavas during post-eruptive
751 degassing: Evidence from trachytic lavas, Rishiri Volcano, Japan. *J. Volcanol. Geotherm.*
752 *Res.* 149, 124–138.

753 Kurzawa, T., König, S., Alt, J.C., Yierpan, A., Schoenberg, R., 2019. The role of subduction
754 recycling on the selenium isotope signature of the mantle: Constraints from Mariana
755 arc lavas. *Chem. Geol.* 513, 239–249.

756 Jenner, F.E., O'Neill, H.S.C., Arculus, R.J. and Mavrogenes, J.A., 2010. The magnetite crisis in
757 the evolution of Arc-related magmas and the initial concentration of Au, Ag and Cu. *J.*
758 *Petrol.* 51, 2445–2464.

759 Lesne, P., Kohn, S. C., Blundy, J., Witham, F., Botcharnikov, R. E., Behrens, H., 2011.
760 Experimental simulation of closed-system degassing in the system basalt-H₂O–CO₂–
761 S–Cl. *J. Petrol.* 52, 1737–1762.

762 Lissner, M., König, S., Luguët, A., le Roux, P.-J., Schuth, S., Heuser, A., le Roex, A.-P., 2014.
763 Selenium and tellurium systematics in MORBs from the southern Mid-Atlantic Ridge
764 (47–50°S). *Geochim. Cosmochim. Acta* 144, 379–402.

765 Lorand J.-P., Alard O., 2010. Determination of selenium and tellurium concentrations in
766 Pyrenean peridotites (Ariege, France): new insight into S/Se/Te systematics of the
767 upper in mantle samples. *Chem. Geol.* 278, 120–130.

768 McPhail, D.C., 1995. Thermodynamic properties of aqueous tellurium species between 25 and
769 350°C. *Geochim. Cosmochim. Acta* 59, 851–866.

770 Merle, R., Caroff, M., Girardeau, J., Cotton, J., Guivel, C., 2005. Segregation vesicles, cylinders,
771 and sheets in vapor-differentiated pillow lavas: examples from Tore-Madeira Rise and
772 Chile Triple Junction, *J. Volcanol. Geotherm. Res.* 141, 109-122.

773 Merle, O., Mairine, P., Michon, L, Bachèlery, P., Smietana, M., 2010. Calderas, landslides and
774 paleo-canyons on Piton de la Fournaise volcano (La Réunion Island, Indian Ocean). *J*
775 *Volcanol. Geotherm. Res.* 189, 131–142.

776 Millner, T., Neugebauer, J., 1949. Volatility of the Oxides of Tungsten and Molybdenum in the
777 Presence of Water Vapour. *Nature*, 163, 601-602.

778 Moussallam, Y., Edmonds, M., Scaillet, B., Peters, N., Gennaro, E., Sides, I., Oppenheimer, C.,
779 2016. The impact of degassing on the oxidation state of basaltic magmas: A case study
780 of Kīlauea volcano. *Earth Planet. Sci. Lett.* 450, 317-325.

781 Nauret, F., Famin, V., Vlastelic, I., Gannoun, A., 2019. A trace of recycled continental crust in
782 the Réunion hotspot. *Chem. Geol.* 524, 67–76.

783 Nougier, J., Cantagrel, J.M., Karche, J.P., 1986. The Comores archipelago in the western Indian
784 Ocean: volcanology, geochronology and geodynamic setting. *J. Afr. Earth Sci.* 1983,
785 135–145.

786 Pelleter, A.-A., Caroff, M., Cordier, C., Bachelery, P., Nehlig, P., Debeuf, D., Arnaud, N., 2014.
787 Melilite-bearing lavas in Mayotte (France): An insight into the mantle source below the
788 Comores. *Lithos* 208–209, 281–297.

789 Peters, B.J., Day, J.M.D., Taylor, L.A., 2016. Early mantle heterogeneities in the Réunion
790 hotspot source inferred from highly siderophile elements in cumulate xenoliths. *Earth*
791 *Planet. Sci. Lett.*, 448, 150-160.

792 Pichavant, M., Brugier, Y., Di Muro, A., 2016. Petrological and Experimental Constraints on the
793 Evolution of Piton de la Fournaise Magmas. In: Bachelery, P., Lenat, JF., Di Muro, A.,
794 Michon, L. (eds) *Active Volcanoes of the Southwest Indian Ocean. Active Volcanoes of*
795 *the World.* Springer, Berlin, Heidelberg.

796 Philpotts, A.R., Lewis, C.L., 1987. Pipe vesicles—An alternate model for their origin. *Geology*
797 15 (10), 971–974.

798 Renggli C.J., Hellmann J.L., Burkhardt C., Klemme S., Berndt J., Pangritz P., Kleine T., 2022.
799 Tellurium isotope fractionation during evaporation from silicate melts, *Geochim.*
800 *Cosmochim. Acta* 339, 35-45.

801 Rinnert, E., Cathalot, C., Feuillet, N., 2021. GEOFLAMME cruise, RV Pourquoi pas ?,
802 <https://doi.org/10.17600/18001297>.

803 Rinnert, E., Lebas, E., Paquet, F., Jorry, S., Feuillet, N., Thinon, I., Fouquet, Y., 2019. MAYOBS
804 cruises, <https://doi.org/10.18142/291>.

805 Rosca C., Vlastélic I., Varas-Reus M.I., König S, 2022. Isotopic constraints on selenium
806 degassing from basaltic magma and near-surface capture by fumarolic deposits:
807 Implications for Se redistribution onto the Earth’s surface. *Chem. Geol.* 596, 120796.

808 Rubin, K., 1997. Degassing of metals and metalloids from erupting seamount and mid-ocean
809 ridge volcanoes: Observations and predictions. *Geochim. Cosmochim. Acta* 61, 3525–
810 3542.

811 Shannon R.D., 1976. Revised effective ionic radii and systematic studies of interatomic
812 distances in halides and chalcogenides. *Acta Cryst.* A32, 751–767.

813 Sharma, V.K., McDonald, T.J., Sohn, M. et al., 2015. Biogeochemistry of selenium. A review.
814 *Environ. Chem. Lett.* 13, 49–58.

815 Smietana, M., Bachèlery, P., Hémond, C., 2010. Heterogeneity in the mantle source of La
816 Réunion Island. In: *Geochim. Cosmochim. Acta*, Goldschmidt conference 2010 abstract
817 74, pp A972.

818 Smietana, M., 2011. *Pétrologie, géochronologie (K–Ar) et géochimie élémentaire et*
819 *isotopique (Sr, Nd, Hf, Pb) de laves anciennes de la Réunion: Implications sur la*
820 *construction de l’édifice volcanique.* PhD thesis, Université de la Réunion.

821 Thinon, I., Lemoine, A., Leroy, S., Paquet, F., Berthod, C., Zaragosi, S., Famin, V., Feuillet, N.,
822 Boymond, P., Masquelet, C., Mercury, N., Rusquet, A., Scalabrin, C., Van der Woerd, J.,
823 Bernard, J., Bignon, J., Clouard, V., Doubre, C., Jacques, E., Jorry, S.J., Rolandone, F.,
824 Chamot-Rooke, N., Delescluse, M., Franke, D., Watremez, L., Bachèlery, P., Michon, L.,
825 Sauter, D., Bujan, S., Canva, A., Dassie, E., Roche, V., Ali, S., Sitti Allaouia, A.H., Deplus,
826 C., Rad, S., Sadeski, L., 2022. Volcanism and tectonics unveiled in the Comoros
827 Archipelago between Africa and Madagascar. *C. R. Géoscience* 354, 1–28.

828 Upton, B.G.J., Wadsworth, W. J., 1972. Aspects of magmatic evolution on Réunion Island.
829 *Philosophical Transactions of the Royal Society of London, Series A* 271, 105–130.

830 Upton B.G.J., Semet M.P., Joron J.-L., 2000. Cumulate clasts in the Bellecombe Ash Member,
831 Piton de la Fournaise, Reunion Island, and their bearing on cumulative processes in the
832 petrogenesis of the Réunion lavas. *J. Volcanol. Geotherm. Res.* 104, 297–318.

833 Verdurme et al., 2024. Magma ascent and lava flow field emplacement during the 2018–2021
834 Fani Maoré deep-submarine eruption insights from lava vesicle textures. *Earth Planet.*
835 *Sci. Lett.* 636, 118720.

836 Villemant, B., Salaün, A., Staudacher, T., 2009. Evidence for a homogeneous primary magma
837 at Piton de la Fournaise (La Réunion): A geochemical study of matrix glass, melt
838 inclusions and Pélé’s hairs of the 1998–2008 eruptive activity. *J. Volcanol. Geotherm.*
839 *Res.* 184, 79–92.

840 Vigouroux, N., Williams-Jones, A. E., Wallace, P., Staudacher, T., 2009. The November 2002
841 eruption of Piton de la Fournaise, Réunion: tracking the pre-eruptive thermal evolution
842 of magma using melt inclusions. *Bull. Volcanol.* 71, 1077-1089.

843 Vlastélic I., Lewin, E., Staudacher, T., 2006. Th/U and other geochemical evidence for the
844 Reunion plume sampling a less differentiated mantle domain. *Earth Planet. Sci. Lett.*
845 248, 364-378.

846 Vlastélic, I., Ménard, G., Gannoun, A., Piro, J.-L., Staudacher, T., Famin, V., 2013. Magma
847 degassing during the April 2007 collapse of Piton de la Fournaise: the record of semi-
848 volatile trace elements (Li, B, Cu, In, Sn, Cd, Re, Tl, Bi). *J. Volcanol. Geotherm. Res.* 254,
849 94–107.

850 Vlastélic, I., Di Muro, A., Bachèlery, P., Gurioli, L., Gannoun, A., Auclair, D., 2018. Control of
851 source fertility on the eruptive activity of Piton de la Fournaise volcano, La Réunion.
852 *Sci. Rep.* 8, 14478.

853 Vlastélic, I., Piro, J.-L., 2022. Volatilization of trace elements during evaporation to dryness of
854 HF-dissolved silicates (BHVO-2, AGV-1, BIR-1, UB-N): Open versus closed system
855 conditions. *Geostand. Geoanal. Res.* 46, 519-534.

856 Wang, Z., Becker, H., 2013. Ratios of S, Se and Te in the silicate Earth require a volatile-rich
857 late veneer. *Nature* 499, 328–331.

858 Wykes, J.L., O'Neill, H.S.C., Mavrogenes, J.A., 2015. The Effect of FeO on the Sulfur Content at
859 Sulfide Saturation (SCSS) and the Selenium Content at Selenide Saturation of Silicate
860 Melts. *J. Petrol.* 56, 1407–1424.

861 Yi, W., Halliday, A. N., Alt, J.C., Lee, D.-C., Rehkämper, M., Garcia, M.O., Langmuir, C.H., Su, Y.,
862 2000. Cadmium, indium, tin, tellurium, and sulfur in oceanic basalts: implications for
863 chalcophile element fractionation in the Earth. *J. Geophys. Res.* 105(B8), 18927-18948.

864 Yierpan, A., König, S., Labidi, J., Kurzawa, T., Babechuk, M. G., Schoenberg, R., 2018. Chemical
865 sample processing for combined selenium isotope and selenium- tellurium elemental
866 investigation of the Earth's igneous reservoirs. *Geochem. Geophys, Geosyst.* 19, 516–
867 533.

868 Yierpan, A., König, S., Labidi, J., Schoenberg, R., 2019. Selenium isotope and S-Se-Te elemental
869 systematics along the Pacific-Antarctic ridge: Role of mantle processes. *Geochim.*
870 *Cosmochim. Acta* 249, 199–224.

- 871 Yierpan, A., Redlinger, J., König, S., 2021. Selenium and tellurium in Reykjanes Ridge and
872 Icelandic basalts: evidence for degassing-induced Se isotope fractionation. *Geochim.*
873 *Cosmochim. Acta* 313, 155–172.
- 874 Zelenski, M., Simakin, A., Taran, Y., Kamenetsky, V.S., Malik, N., 2021. Partitioning of elements
875 between high-temperature, low-density aqueous fluid and silicate melt as derived
876 from volcanic gas geochemistry. *Geochim. Cosmochim. Acta* 295, 112–134.

Table 1: Samples type and location

Site	Volcano	Sample	Composition	Sample type	Location / eruption phase	Lat. °S	Long. °E	Elevation (m)
Reunion	PdN subaerial	CB2150914	Wehrlite	Cumulate	LM	-21.07	55.50	876
		SAL 206	Wehrlite	Cumulate	Phase I	-21.08	55.50	1077
		BSUZ 2	SSB	Lava flow	Phase I	-21.00	55.42	500
		SAL 51	SSB	Dyke in breccia	Phase I	-21.06	55.49	830
		SAL 48	SSB	Dyke in breccia	Phase I	-21.06	55.49	830
		RUN 008-2006	Hawaiite	Lava flow	Phase III	-21.12	55.27	220
		RUN 038-2006	Benmoreite	Lava flow	Phase IV	-21.09	55.55	1505
		RUN 048-2006	Benmoreite	Lava flow	Phase IV	-21.07	55.38	2020
		SAB 1	Trachyte	Dyke	Phase IV	-21.07	55.47	1710
		SAL 88	Trachyte	Sill in breccia	Phase IV	-21.06	55.51	858
		SAL 200	Trachyte	Sill in breccia	Phase IV	-21.07	55.50	820
		SAL 203	Trachyte*	Sill in breccia	Phase IV	-21.06	55.49	880
		SAL 201	Trachyte*	Sill in breccia	Phase IV	-21.07	55.50	890
		PdF subaerial	CHI-7	Wehrlite	Peridotite	Piton Chisny	-21.24	55.67
	REU 070402-1b		SSB	Lava flow	April 2007 eruption	-21.28	55.77	580
	REU 070403-b		SSB	Lava flow	April 2007 eruption	-21.28	55.77	580
	REU 070404-b		SSB	Lava flow	April 2007 eruption	-21.28	55.77	580
	REU 070408-1b		Olivine-rich basalt	Lava flow	April 2007 eruption	-21.28	55.77	580
	REU 150731-7		SSB	Golden pumice	July 2015 eruption	-21.22	55.71	2139
	REU 180413-1		SSB	Lava crust	April 2018 eruption	-21.21	55.72	1920
	REU 180403		SSB	Scoria	April 2018 eruption	-21.21	55.72	1920
	REU 180713-1		SSB	Lava, water quenched	July 2018 eruption	-21.23	55.70	2230
	REU 200409-6		SSB	Pele hairs	April 2020 eruption	-21.23	55.66	2269
	PdN submarine	ERO2 DR6-2	SSB	Pillow lava	Etang Salé Ridge, 2.48 Ma	-21.35	55.24	-2000
		ERO2 DR7-4B	SSB	Pillow lava	Etang Salé Ridge	-21.35	55.24	-1780
		ERO2 DR7-3	SSB	Pillow lava	Etang Salé Ridge	-21.35	55.24	-1780
		ERO2 DR7-5	SSB	Pillow lava	Etang Salé Ridge	-21.35	55.24	-1780
	PdF submarine	ERO2 DR2-6	SSB	Pillow lava	North of PdF NE Rift Zone, 3.34 Ma	-21.09	55.86	-1700
		GSR2-DR11-47	Mg-rich basalt	Pillow lava	North of PdF NE Rift Zone, 3.77 Ma	-21.09	55.86	-1850
		ERO2 DR8-7	Mg-rich basalt	Pillow lava	South of PdF NE Rift Zone, 0.439 Ma	-21.20	55.91	-1443
		ERO2 DR8-1	Mg-rich basalt	Pillow lava	South of PdF NE Rift Zone, 0.439 Ma	-21.20	55.91	-1443
		ERO2 DR8-6	Mg-rich basalt	Pillow lava	South of PdF NE Rift Zone, 0.439 Ma	-21.20	55.91	-1443
		ERO2 DR8-8	Mg-rich basalt	Pillow lava	South of PdF NE Rift Zone, 0.439 Ma	-21.20	55.91	-1443
	Mayotte	Fani Maoré	MAY01-DR01-05	Evolved basanite	Pillow lava	Phase 1 (July 2018 - May 2019)	-12.91	45.72
MAY02-DR08-01ALF			Evolved basanite	Pillow lava	Phase 2 (May 2019 - August 2019)	-12.94	45.71	-3061
MAY02-DR08-0102MB			Evolved basanite	Pillow lava	Phase 2 (May 2019 - August 2019)	-12.94	45.71	-3061
MAY04-DR10-07			Evolved basanite	Pillow lava	Phase 1 (July 2018 - May 2019)	-12.92	45.72	-3035
MAY04-DR11-0704-2			Evolved basanite	Pillow lava	Phase 2 (May 2019 - August 2019)	-12.92	45.69	-3239
MAY04-DR12-0301			Evolved basanite	Pillow lava	Phase 1 (July 2018 - May 2019)	-12.88	45.72	-3222
MAY04-DR11-0704			Evolved basanite	Pillow lava	Phase 2 (May 2019 - August 2019)	-12.92	45.69	-3239
GFL-DR20-0101			Evolved basanite	Pillow lava	Phase 3b (October 2020 - January 2021)	-12.87	45.67	-3179

SSB : Steady State Basalts. Most common basalts at La Réunion Island, with composition transitionnal between tholeiites and alkali basalts

PdN : Piton des Neiges. PdF : Piton de la Fournaise.

* With hydrothermal pyrite

Table 2: S, Se and Te concentrations of reference materials and rock samples from La Réunion island and Fani Maoré volcano, Mayotte.

Site	Volcano	Sample	MgO (wt%)	[S] ppm	SD	[Se] ppb	SD	[Te] ppb	SD
		BHVO-2		185 ±	7 (n=10)	170 ±	11 (n=20)	14.52 ±	0.77 (n=14)
		BCR-2		341 ±	1 (n=2)	79.6 ±	0.8 (r=3)	2.84 ±	0.07 (r=3)
		BE-N		336 ±	5 (r=1)	71.7 ±	0.9 (r=1)	1.06 ±	0.01 (r=2)
		BIR-1		4.43 ±	0.04 (r=3)	16.1 ±	0.04 (r=2)	5.90 ±	0.06 (r=1)
La Réunion	PdN subaerial	CB2150914	33.0	358 ±	1.9	35.9 ±	1.2	2.72 ±	0.04
		SAL 206	41.5	264 ±	2.8	18.9 ±	0.6	3.11 ±	0.05
		BSUZ 2	6.5	30 ±	0.2	71.0 ±	2.4	0.38 ±	0.02
		SAL 51	6.7	257 ±	2.5	132 ±	4.2	8.76 ±	0.07
		SAL 48	8.2	141 ±	1.1	93.4 ±	3.3	2.95 ±	0.04
		RUN 008-2006	4.4	28 ±	0.3	37.9 ±	1.3	0.25 ±	0.02
		RUN 038-2006	1.4	10 ±	0.2	3.0 ±	0.2	0.46 ±	0.02
		RUN 048-2006	2.4	40 ±	0.3	11.6 ±	0.4	1.00 ±	0.03
		SAB 1	0.4	4.9 ±	0.1	2.0 ±	0.2	0.27 ±	0.01
		SAL 88	0.6	-		0.7 ±	0.1	0.19 ±	0.02
		SAL 200	2.3	168 ±	1.2	23.0 ±	0.9	0.64 ±	0.03
		SAL 203	2.8	730 ±	5.4	75.8 ±	2.5	1.30 ±	0.02
		SAL 201	4.4	884 ±	11	206 ±	5.0	2.47 ±	0.03
		PdF subaerial	CHI-7	33.4	13 ±	0.1	10.0 ±	0.4	2.56 ±
	070402-1b		7.3	101 ±	1.6	124 ±	2.7	2.16 ±	0.21
	070403-b		7.5	266 ±	1.8	130 ±	2.9	1.54 ±	0.15
	070404-b		7.3	102 ±	1.2	134 ±	2.7	1.07 ±	0.11
	070408-1b		29.2	24 ±	0.3	59.3 ±	1.0	0.69 ±	0.09
	150731-7		6.4	245 ±	3.1	131 ±	2.7	0.74 ±	0.01
	180413-1		6.9	199 ±	2.5	134 ±	2.9	0.87 ±	0.09
	180403		6.9	210 ±	2.8	133 ±	2.2	1.53 ±	0.17
	180713-1		6.9	147 ±	0.6	127 ±	2.7	0.56 ±	0.05
	200409-6		8.0	196 ±	0.8	677 ±	10	120 ±	6
	PdN submarine		DR6-2	7.6	416 ±	1.7	96.7 ±	2.4	3.73 ±
		DR7-4B	5.1	119 ±	0.7	51.0 ±	2.1	22.8 ±	0.79
		DR7-3	6.2	437 ±	4.3	112 ±	2.9	61.6 ±	4.88
		DR7-5	5.5	146 ±	0.8	33.8 ±	1.1	33.0 ±	0.63
	PdF submarine	DR2-6	6.7	165 ±	1.0	74.3 ±	1.8	9.54 ±	0.52
		GSR2-DR11-47	10.5	564 ±	3.0	116 ±	5.4	4.47 ±	0.21
		DR8-7	10.9	632 ±	7.5	125 ±	2.6	6.95 ±	0.07
		DR8-1	13.1	551 ±	5.8	112 ±	2.4	12.4 ±	0.55
DR8-6		9.6	502 ±	4.0	109 ±	3.1	3.71 ±	0.02	
DR8-8	12.0	435 ±	4.9	89.9 ±	1.8	6.04 ±	0.26		
Mayotte	Fani Maoré	MAY01-DR01-05	4.77	1342 ±	32	76.7 ±	1.1	6.15 ±	0.06
		MAY02-DR08-01ALF	3.77	1509 ±	40	68.2 ±	1.1	9.53 ±	0.07
		MAY02-DR08-0102MB	3.79	1454 ±	32	69.4 ±	1.0	13.6 ±	0.10
		MAY04-DR10-07	4.18	1413 ±	41	72.8 ±	1.0	6.26 ±	0.05
		MAY04-DR11-0704-2	3.97	1386 ±	32	66.5 ±	1.2	4.43 ±	0.06
		MAY04-DR12-0301	4.52	1367 ±	39	80.7 ±	1.3	5.71 ±	0.06
		MAY04-DR11-0704	9.89	1430 ±	25	67.3 ±	1.1	5.48 ±	0.06
	GFL-DR20-0101 Bulk	4.45	1711		81.5		5.23		
	drilling	distance to pillow rim							
	DR20-1	21.3 cm	1794 ±	30	83.5 ±	2.1	4.89 ±	0.05	
	DR20-3	17.5 cm	1671 ±	26	82.6 ±	2.0	4.79 ±	0.06	
	DR20-5	13.5 cm	1593 ±	47	76.8 ±	1.7	4.70 ±	0.06	
	DR20-7	9.5 cm	1518 ±	37	77.0 ±	2.0	4.47 ±	0.05	
	DR20-9	5.5 cm	1625 ±	34	81.4 ±	1.6	4.87 ±	0.05	
	DR20-10	3.5 cm	1768 ±	49	83.2 ±	1.7	5.75 ±	0.06	
	DR20-11	2 cm	1751 ±	35	82.1 ±	1.4	5.94 ±	0.06	
	DR20-12	1 cm	1801 ±	35	83.6 ±	1.6	6.04 ±	0.08	
DR20-SP	0 cm	1881 ±	30	83.1 ±	1.8	5.65 ±	0.07		

n: dissolution & chemistry duplicate

r: analysis replicate (same solution)

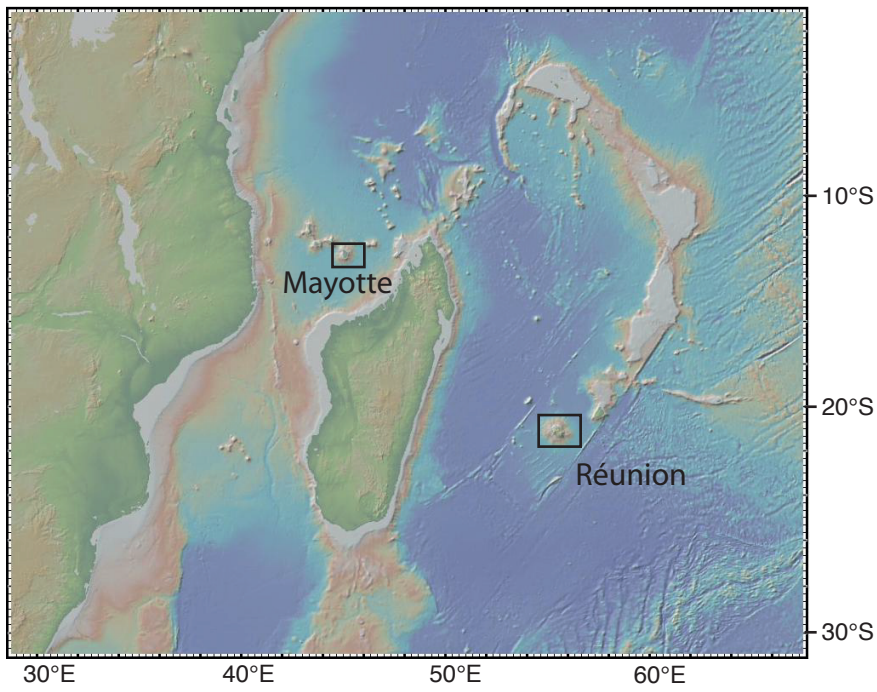
SD: sample SD is calculated by propagating errors on isotopic ratios (see text)

MgO data are from the supplementary table S1 (La Reunion) and from Berthod et al. (2022)

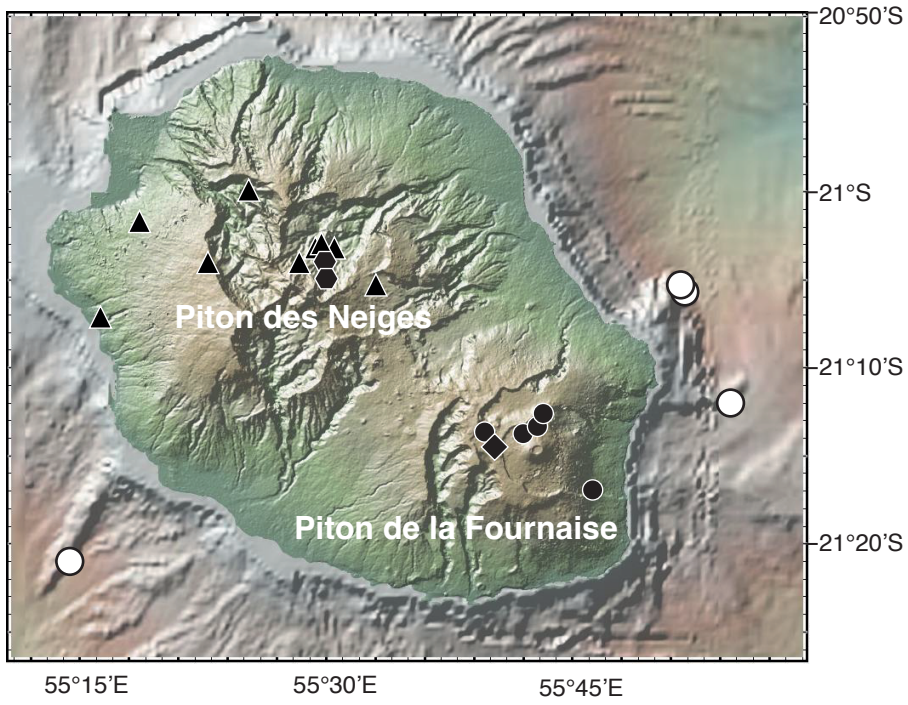
PdN: Piton des Neiges. PdF: Piton de la Fournaise.

F1

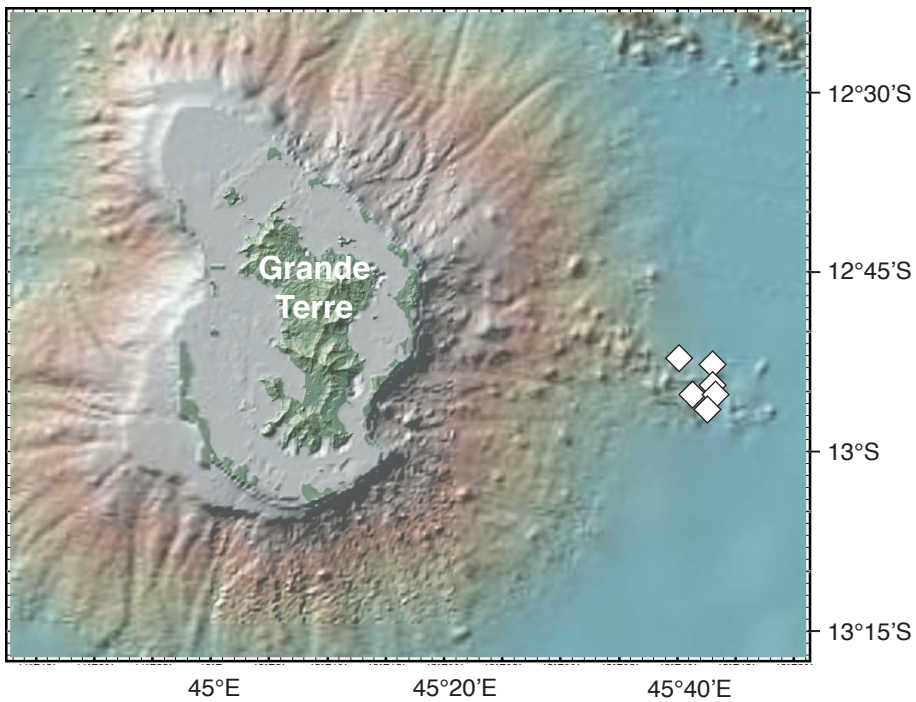
A)



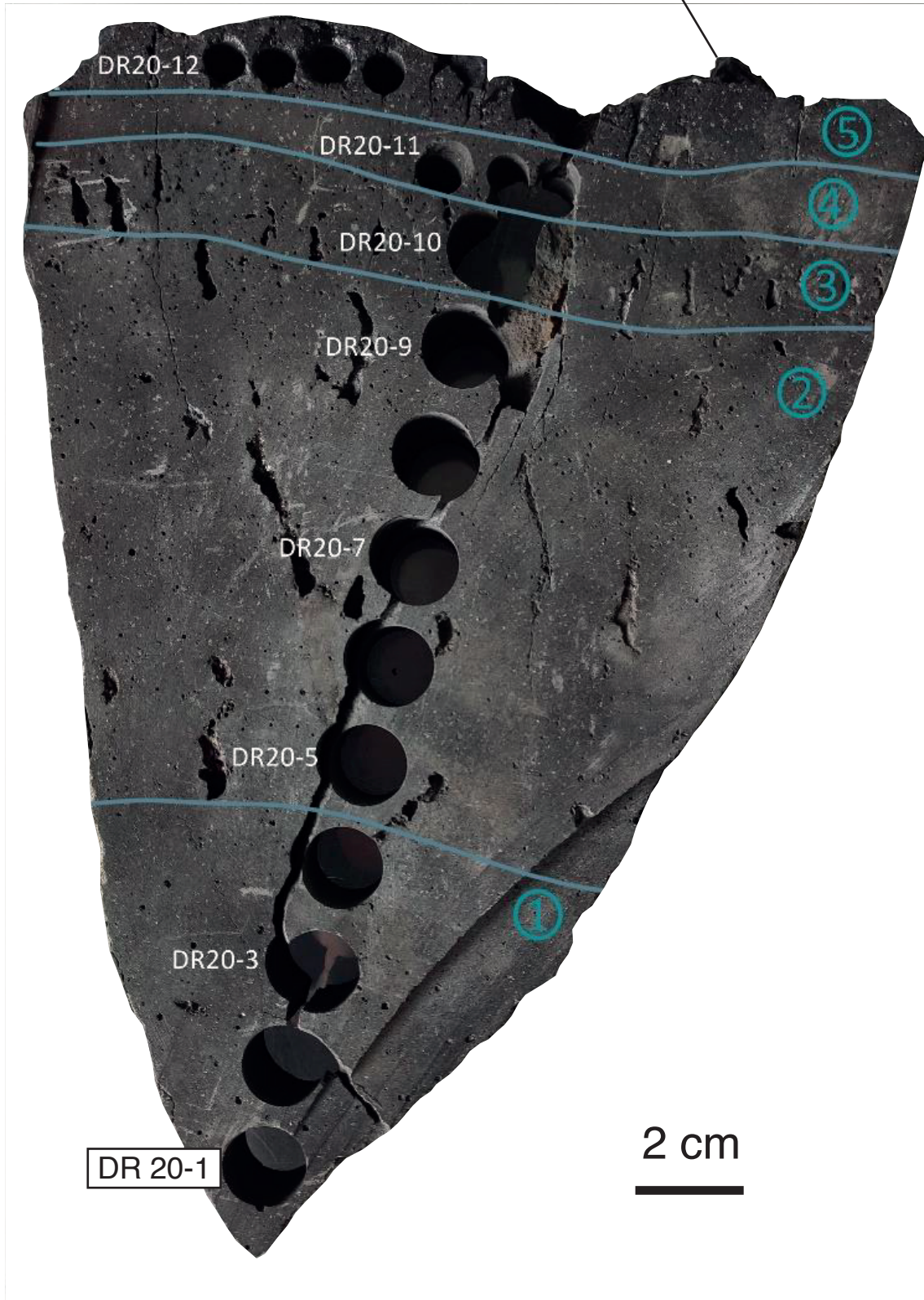
B)

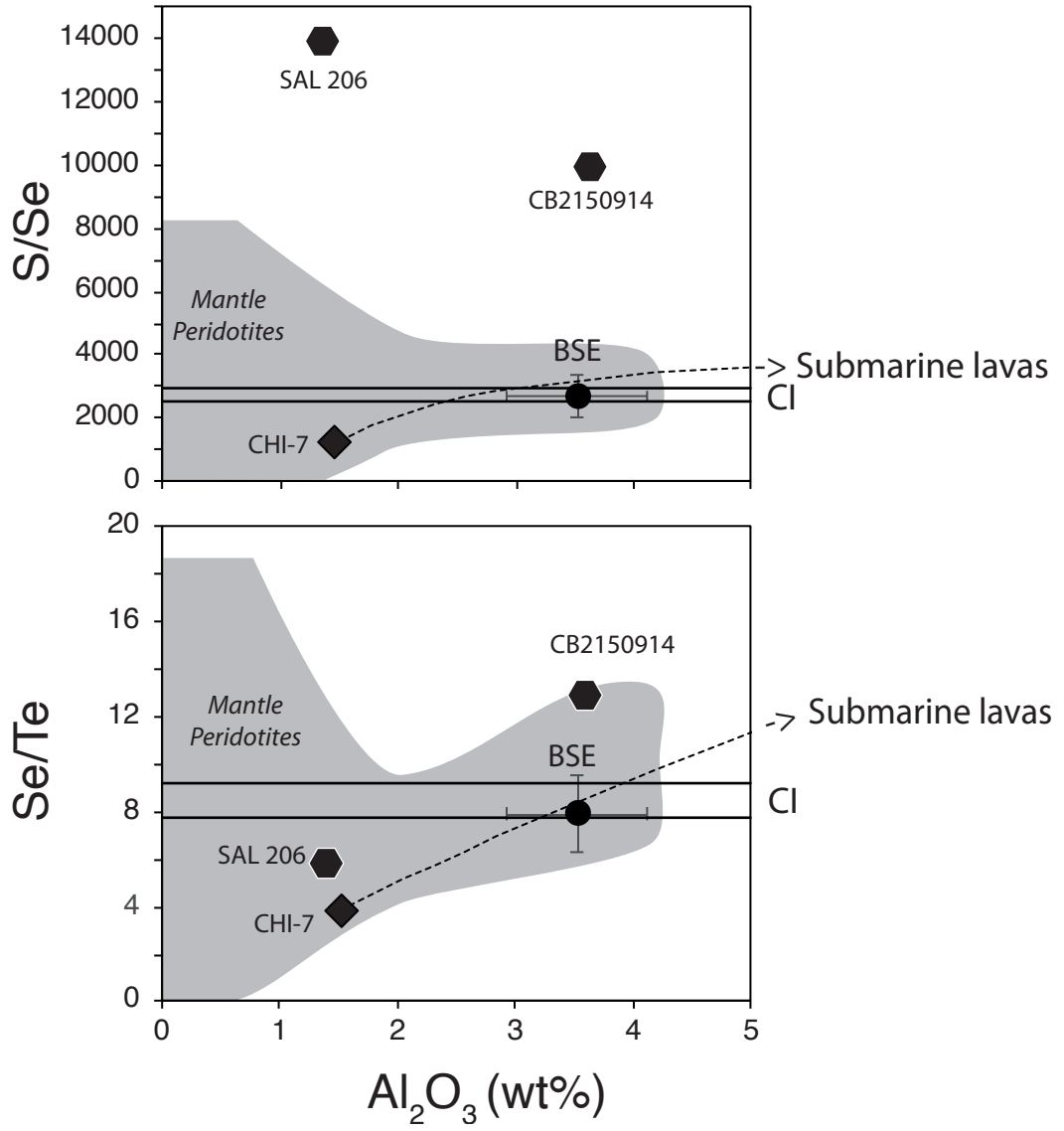


C)



DR20-Sp
(Layer 6 : thin glassy crust)





Crystallization assemblage**La Réunion**

(1) Ol + Spl

(2) Ol + Cpx + Plg + Spl

(3) Cpx + Plg + Sulf

(4) Cpx + Plg + Mnt + Sulf

Fani Maoré eruption (Mayotte)

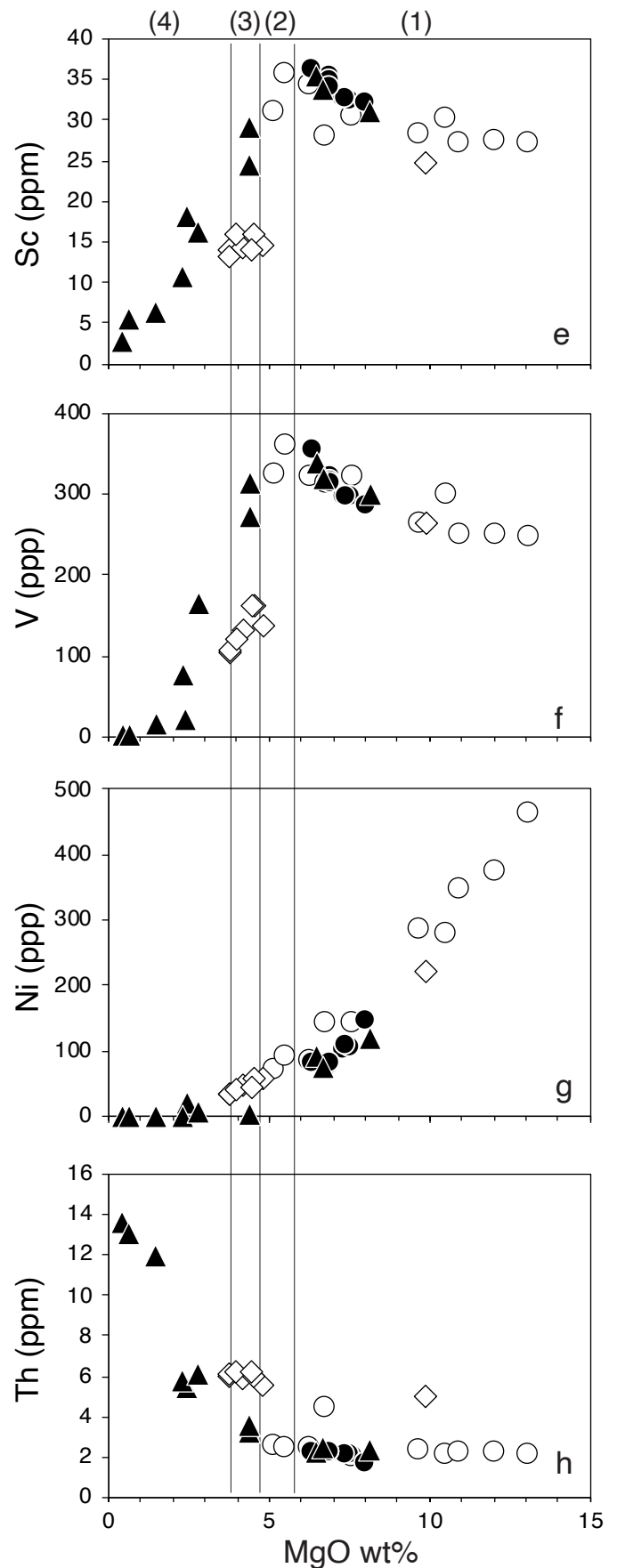
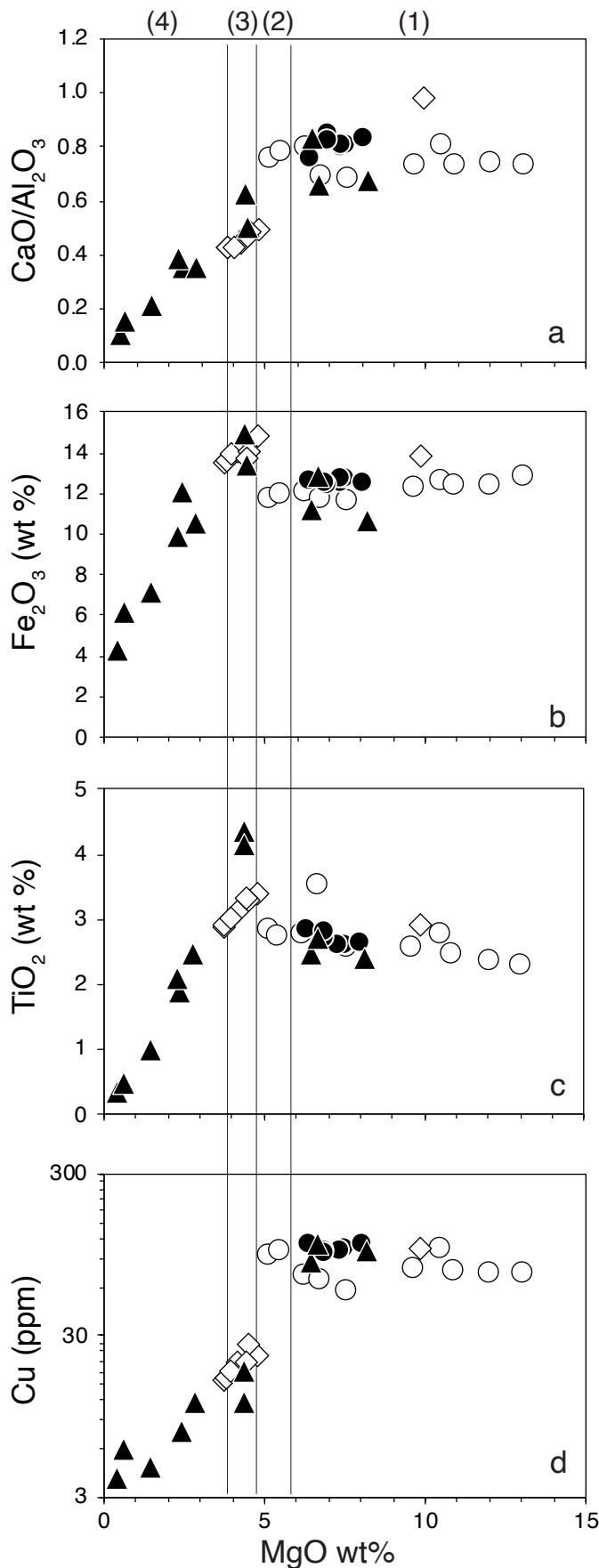
(2-3) 80% Cpx + 20% Ol + Sulf

○ La Réunion submarine lavas

● Piton de la Fournaise lavas

▲ Piton des Neiges lavas

◇ Fani Maoré submarine eruption



Crystallization assemblage

La Réunion

- (1) Ol + Spl
- (2) Ol + Cpx + Plg + Spl
- (3) Cpx + Plg + Sulf
- (4) Cpx + Plg + Mnt + Sulf

Fani Maoré eruption (Mayotte)

- (2-3) 80% Cpx + 20% Ol + Sulf

- La Reunion submarine lavas
- Piton de la Fournaise lavas
- P.H. PdF Pele's Hairs
- ▲ Piton des Neiges lavas
- ▲ Piton des Neiges lavas with pyrite
- ◇ Mayotte submarine lavas

